

# *The asymmetric eddy-background flow interaction in the North Pacific storm track*

Article

Accepted Version

Zhao, Y.-B., Liang, X. S., Guan, Z. and Hodges, K. I. ORCID: <https://orcid.org/0000-0003-0894-229X> (2019) The asymmetric eddy-background flow interaction in the North Pacific storm track. *Quarterly Journal of the Royal Meteorological Society*, 145 (719). pp. 575-596. ISSN 1477-870X doi: <https://doi.org/10.1002/qj.3453> Available at <https://centaur.reading.ac.uk/80948/>

It is advisable to refer to the publisher's version if you intend to cite from the work. See [Guidance on citing](#).

To link to this article DOI: <http://dx.doi.org/10.1002/qj.3453>

Publisher: Royal Meteorological Society

All outputs in CentAUR are protected by Intellectual Property Rights law, including copyright law. Copyright and IPR is retained by the creators or other copyright holders. Terms and conditions for use of this material are defined in the [End User Agreement](#).

[www.reading.ac.uk/centaur](http://www.reading.ac.uk/centaur)

**CentAUR**

Central Archive at the University of Reading

Reading's research outputs online

**The asymmetric eddy-background flow interaction in the  
North Pacific storm track**

Journal:	<i>QJRMS</i>
Manuscript ID	QJ-18-0042.R2
Wiley - Manuscript type:	Research Article
Date Submitted by the Author:	n/a
Complete List of Authors:	Zhao, Yuan-Bing; Nanjing University of Information Science and Technology, Liang, X. San; Nanjing University of Information Science and Technology Guan, Zhaoyong; Nanjing University of Information Science and Technology Hodges, Kevin; The University of Reading, Dept. of Meteorology
Keywords:	eddy-mean flow interaction, extra-tropical cyclone, feature tracking, multiscale energetics, canonical energy transfer
Country Keywords:	China

1  
2  
3  
4  
5 1 **The asymmetric eddy-background flow interaction in the North Pacific storm track**  
6  
7

8  
9 2 **Yuan-Bing Zhao<sup>1</sup>, X. San Liang<sup>12\*</sup>, Zhaoyong Guan<sup>1</sup>, and Kevin I. Hodges<sup>3</sup>**  
10

11  
12 3  
13  
14 4 <sup>1</sup> School of Atmospheric Sciences, Nanjing University of Information Science and  
15  
16 5 Technology, Nanjing, Jiangsu, 210044, China

17  
18  
19 6 <sup>2</sup> School of Marine Sciences, Nanjing University of Information Science and Technology,  
20  
21 7 Nanjing, Jiangsu, 210044, China

22  
23  
24 8 <sup>3</sup> Department of Meteorology, National Centre for Earth Observation, University of  
25  
26 9 Reading, Reading, UK  
27  
28  
29

30 10

31  
32 11 **Correspondence**  
33

34  
35 12 X. San Liang, Nanjing Center for Ocean-Atmosphere Dynamical Studies, Nanjing,  
36  
37 13 Jiangsu, 210044, China.

38  
39  
40 14 E-mail: [x.san.liang@gmail.com](mailto:x.san.liang@gmail.com)  
41  
42

43 15

44  
45 16 **Running head**  
46

47  
48 17 Asymmetric eddy-mean flow interaction  
49

50  
51 18  
52

53 19  
54  
55  
56  
57  
58  
59  
60

1  
2  
3  
4 **20 Abstract**  
5

6  
7 21 Using a recently developed methodology, namely, the multiscale window transform  
8  
9 22 (MWT), and the MWT-based theory of canonical transfer and localized multiscale  
10  
11 23 energetics analysis, we investigate in an eddy-following way the nonlinear  
12  
13 24 eddy-background flow interaction in the North Pacific storm track, based on the ERA40  
14  
15 25 reanalysis data from ECWMF. It is found that more than 50% of the storms occur on the  
16  
17 26 northern flank of the jet stream, about 40% are around the jet center, and very few (less  
18  
19 27 than 5%) happen on the southern flank. For storms near or to the north of the jet center,  
20  
21 28 their interaction with the background flow is asymmetric in latitude. In higher latitudes,  
22  
23 29 strong downscale canonical available potential energy transfer happens, especially in the  
24  
25 30 middle troposphere, which reduces the background baroclinicity and decelerates the jet;  
26  
27 31 in lower latitudes, upscale canonical kinetic energy transfer intensifies at the jet center,  
28  
29 32 accelerating the jet and enhancing the middle-level baroclinicity. The resultant effect is  
30  
31 33 that the jet strengthens but narrows, leading to an anomalous dipolar pattern in the fields  
32  
33 34 of background wind and baroclinicity. For the storms on the southern side of the jet, the  
34  
35 35 baroclinic canonical transfer is rather weak. On average, the local interaction begins from  
36  
37 36 about 3 days before a storm arrives at the site of observation, achieves its maximum as  
38  
39 37 the storm arrives, and then weakens.  
40  
41  
42  
43  
44  
45  
46  
47  
48  
49

50  
51 38

52  
53 39 **KEYWORDS**  
54  
55  
56  
57  
58  
59  
60

1  
2  
3  
4 40 Eddy-mean flow interaction, extra-tropical cyclone, feature tracking, multiscale  
5  
6  
7 41 energetics, canonical energy transfer  
8

9 42

## 11 43 **1. Introduction**

14 44 Eddy-mean flow interaction is one of the central issues in dynamical meteorology.  
15  
16  
17 45 In the atmosphere, a typical site of eddy-mean flow interaction is the midlatitude storm  
18  
19  
20 46 track (Blackmon, 1976; Chang and Orlanski, 1993; Hoskins and Valdes, 1990). It has  
21  
22  
23 47 been shown that the atmospheric storm track generally coincides with the tropospheric  
24  
25  
26 48 jet, where the baroclinicity is the strongest (e.g., Chang et al., 2002; Lee and Kim, 2003).  
27  
28  
29 49 Within the storm track, synoptic eddies are often generated in the jet and then interact  
30  
31 50 with it.

32  
33 51 There is a long history of studies on the interaction between midlatitude synoptic  
34  
35  
36 52 eddies and the jet stream. In most early studies, the focus was on the theoretical aspects  
37  
38  
39 53 based on idealized models, e.g., those with small-amplitude perturbations in the form of  
40  
41  
42 54 sinusoidal waves and a zonally homogeneous, stationary background flow (in many cases  
43  
44  
45 55 also meridionally independent) (Andrews and McIntyre, 1978; Charney and Drazin,  
46  
47  
48 56 1961; Dickinson, 1969; Eliassen and Palm, 1961; Lindzen and Holton, 1968; Plumb,  
49  
50  
51 57 1985). However, in the real atmosphere the background flow is by nature temporally  
52  
53  
54 58 varying and zonally asymmetric; especially in midlatitudes, due to the large scale  
55  
56  
57 59 topography and land-sea contrasts (e.g., Lee and Kim, 2003; Li and Wettstein, 2011),  
58  
59  
60 60 whilst the eddies are rather localized in space and time with finite amplitudes (Blackmon

1  
2  
3  
4 61 et al., 1984; Catto et al., 2010; Chang, 1993; Lim and Wallace, 1991; Simmons and  
5  
6  
7 62 Hoskins, 1978). In more recent studies, with the advent of observational and reanalysis  
8  
9  
10 63 data, discrepancies have been found between the previously proposed theories and the  
11  
12 64 observations. For example, based on the previous theories it is supposed that baroclinic  
13  
14 65 energy transfer associated with baroclinic instability is bottom-trapped (Edmon et al.,  
15  
16  
17 66 1980; Green, 1960; Hoskins et al., 1985; Lindzen and Farrell, 1980; Pierrehumbert and  
18  
19  
20 67 Swanson, 1995), whereas observational energetics diagnostics have implied that  
21  
22 68 midlatitude synoptic systems have their maximum baroclinic energy transfer in middle  
23  
24  
25 69 levels (e.g., Chang et al., 2002). The spatial structure of the interaction is still a problem  
26  
27  
28 70 yet to be explored.

30 71 During the past two decades, eddy-mean flow interaction has been extensively  
31  
32 72 discussed, especially in studies of annular modes (Barnes and Hartmann, 2011; Burrows  
33  
34  
35 73 et al., 2017; Chen and Plumb, 2009; Gerber and Vallis, 2007; Kidston et al., 2010;  
36  
37  
38 74 Kidston and Vallis, 2012; Lorenz, 2014; Lorenz and Hartmann, 2001; Robinson, 2000;  
39  
40  
41 75 Zhang et al., 2012, to name but a few). But, most of these studies have focused on the  
42  
43  
44 76 zonal-mean and climatologically statistical aspects. Rarely considered is the interaction  
45  
46  
47 77 between a typical individual eddy and the mean flow, except for a few studies such as  
48  
49  
50 78 Gerber and Vallis (2007), who argued that if the eddy is generated in the jet, the vertical  
51  
52  
53 79 wind shear is first reduced by the heat flux in the baroclinic development stage, and then  
54  
55  
56 80 in the decaying stage the jet is strengthened by upgradient momentum transfer through  
57  
58  
59 81 the wave meridional propagation (the net propagation of baroclinic wave activity away  
60

1  
2  
3  
4 82 from the jet gives momentum fluxes into the jet). On the whole, the jet structure is  
5  
6  
7 83 maintained in the presence of surface friction. Alternatively, if the eddy is growing on the  
8  
9  
10 84 shoulders of the jet, the baroclinic development stage is similar to that of the eddy  
11  
12 85 growing in the jet. However, the meridional wave propagation is then limited aloft, and,  
13  
14 86 as a result, the shear is reduced locally rather than over the entire baroclinic zone. Similar  
15  
16  
17 87 studies are also reported in Zhang et al. (2012) based on an idealized  $\beta$ -plane  
18  
19  
20 88 quasi-geostrophic model. As remarked by Vallis and Gerber (2008), the applicability of  
21  
22 89 these results to the real atmosphere still needs verification.

23  
24  
25 90 We remark that, earlier on, a classical way to look at the eddy-mean flow interaction  
26  
27  
28 91 is with the “barotropic generation rate (Mak and Cai 1989; Cai and Mak 1990; Rivière et  
29  
30  
31 92 al. 2003) and “baroclinic generation rate” (Cai and Mak 1990; Rivière et al. 2004). The  
32  
33  
34 93 merit of this method is that if the eddy structure, the deformation of the jet, and the  
35  
36  
37 94 positional relationship between the eddy and the jet are known, then the energy exchange  
38  
39  
40 95 between the jet and the eddy can be easily determined (especially with the barotropic  
41  
42  
43 96 generation rate). But here this method is difficult to be applied, as it is derived in the  
44  
45  
46 97 quasi-geostrophic (QG) framework with the small amplitude assumption; besides, it does  
47  
48  
49 98 not tell how eddies would modify the mean flow.

50  
51 99 In this study we apply a newly developed methodology, which is capable of  
52  
53  
54 100 handling these nonlinear problems in a generic sense, to diagnose the two-way  
55  
56  
57 101 interactions between individual midlatitude synoptic eddies and the background flow in  
58  
59  
60 102 an eddy-following way, in the hope of unraveling what is really happening locally in the



1  
2  
3  
4 103 North Pacific storm track. The methodology includes a functional analysis apparatus,  
5  
6  
7 104 namely, the Multiscale Window Transform (MWT, Liang and Anderson 2007), and the  
8  
9  
10 105 MWT-based localized multiscale energy and vorticity analysis (MS-EVA, Liang 2016).

11  
12 106 The rest of this paper is organized as follows. Section 2 describes the data used in  
13  
14  
15 107 this study. In section 3, we briefly introduce the MWT, MS-EVA, and the Lagrangian  
16  
17  
18 108 tracking and compositing method, and in section 4, we set up the MS-EVA application  
19  
20  
21 109 with the data. In the following sections (5, 6, 7, and 8), the composite reconstructed fields  
22  
23  
24 110 and a detailed eddy-mean flow interaction analysis are presented. The study is  
25  
26  
27 111 summarized in section 9.

## 112 2. Data

113  
114 We use for our study the 40-year European Centre for Medium-Range Weather  
115  
116 Forecasts (ECWMF) ReAnalysis (ERA40) dataset (Uppala et al., 2005), which is  
117  
118 constrained by observations using a three-dimensional variational (3D-Var) data  
119  
120 assimilation system. It has been used because of its length (45 years), spatial resolution  
121  
122 (approximately  $1.1^\circ \times 1.1^\circ$  in the tropics (T159), 35 vertical levels below 100 hPa), and  
123  
124 temporal resolution (6 h). More information can be found at  
125  
126 <http://apps.ecmwf.int/datasets/data/era40-daily/levtype=pl/>. Here we need the velocity  
127  
128 components ( $u$ ,  $v$ , and  $\omega$ ), geopotential ( $\phi$ ), and temperature ( $T$ ) for the whole period  
129  
130 from September 1957 to July 2002.

### 122 3. Methodology

#### 123 3.1 Localized multiscale energetics analysis

124 The major research methodology for this study is the multiscale window transform  
125 (MWT) by Liang and Anderson (2007), and the MWT-based theory of canonical transfer  
126 (Liang 2016) and localized multiscale energy and vorticity analysis (MS-EVA) by Liang  
127 and Robinson (2005), which has been applied successfully in many atmosphere-ocean  
128 problems (e.g., Ma and Liang, 2017; Xu and Liang 2017). This section is just a short  
129 introduction of the concepts; more details are furnished in Appendix A. For a recently  
130 updated comprehensive introduction, refer to Liang (2016).

131 The MWT is a functional analysis tool that helps decompose a function space into a  
132 direct sum of several mutually orthogonal subspaces, each with an exclusive range of  
133 time scales, while preserving its local properties. Such a subspace is termed a *scale*  
134 *window* or simply a *window*. One may have as many windows as needed. In this study,  
135 we mainly use two, namely, a low-frequency basic-flow window (or background flow  
136 window) and a synoptic-scale window (or transient window); we will also use a  
137 three-window decomposition for testing purpose. For easy reference, they are denoted  
138 and will be referred to as windows  $\varpi = 0, 1, \dots$ . Given a time series  $T(t)$  with  $N$  steps,  
139 application of MWT yields two types of quantities: one is the MWT transform  
140 coefficients,  $\hat{T}_n^{\sim\varpi}$  ( $n = 1, 2, \dots, N$ , corresponding to the time location in  $t$ ), another the  
141 multiscale window reconstruction (MWR),  $T^{\sim\varpi}(t)$ .  $T^{\sim\varpi}(t)$  is just like the

1  
2  
3  
4 142 low/high-pass filtered quantity. For example, in the two-window decomposition in this  
5  
6 143 study, the series  $T(t)$  is decomposed into  $T = T^{\sim 0}(t) + T^{\sim 1}(t)$ , where  $T^{\sim 0}$  stands for  
7  
8 144 the background field, and  $T^{\sim 1}$  the transient (or synoptic) eddy field. MWT and MWR  
9  
10 145 form a transform-reconstruction pair, but they are distinctly different concepts, with the  
11  
12 146 former defined in phase space while the latter in physical space (here  $t$ ), just like the  
13  
14 147 Fourier transform and inverse Fourier transform. The MWR of  $T(t)$  on the synoptic-scale  
15  
16 148 window, for example, corresponds to a high-pass filtered signal. The lack of transform  
17  
18 149 coefficient  $\hat{T}_n^{\sim \varpi}$  in traditional filters makes it impossible to represent multiscale energy<sup>1</sup>.  
19  
20  
21  
22  
23  
24  
25 150 **The common practice that simply takes multiscale energy as the square of filtered**  
26  
27 151 **variables** is a conceptual mistake which, unfortunately, has frequently appeared in the  
28  
29 152 literature. But here with  $\hat{T}_n^{\sim \varpi}$  it has been established that multiscale energy can be  
30  
31 153 precisely represented as the product of the MWT coefficients (up to some constant  
32  
33 154 multiplier). For example, the transient eddy energy extracted from  $T(t)$  is simply  $(\hat{T}_n^{\sim 1})^2$   
34  
35 155 multiplied by some constant.  
36  
37  
38  
39

40 With MWT, the available potential energy (APE) and kinetic energy (KE) densities  
41  
42 156 on window  $\varpi$  at time location  $n$ , written as  $A_n^{\varpi}$  and  $K_n^{\varpi}$ , can be obtained, and their  
43  
44 157 evolution equations derived by applying MWT to the primitive governing equations.  
45  
46 158 Details are referred to Appendix A; the following is a symbolic representation (location  $n$   
47  
48 159 in the subscript omitted henceforth for simplicity):  
49  
50  
51 160

---

52  
53  
54 <sup>1</sup> Note one cannot write it in terms of the filtered quantities such as  $[T^{\sim 1}(t)]^2$ , as multiscale energy is  
55 a concept in phase space. (Think about that in a Fourier spectrum.) Refer to Appendix A for more  
56 explanation.  
57

$$\frac{\partial A^\varpi}{\partial t} + \nabla \cdot \mathbf{Q}_A^\varpi = \Gamma_A^\varpi - b^\varpi + S_A^\varpi + F_A^\varpi \quad (1)$$

$$\frac{\partial K^\varpi}{\partial t} + \nabla \cdot \mathbf{Q}_K^\varpi = \Gamma_K^\varpi - \nabla \cdot \mathbf{Q}_P^\varpi + b^\varpi + F_K^\varpi \quad (2)$$

161 where  $\varpi = 0$  and 1 stand for the two scale windows in this study, i.e., the basic flow  
 162 window and the eddy window. The  $\mathbf{Q}$ 's with subscripts A, K, and P are, respectively,  
 163 fluxes of APE, KE, and pressure, the  $\Gamma$  terms are the transfer of energy (APE or KE) to  
 164 the designated scale window  $\varpi$  from other windows,  $b$  is buoyancy conversion, and  $F$   
 165 denotes the contribution from dissipation/diffusion. Explicit expressions and detailed  
 166 physical interpretations are referred to Appendix A, Table A.1. Note that all the terms are  
 167 localized both in space and in time; in other words, they are all four-dimensional field  
 168 variables, distinguished notably from the classical formalisms in which localization is lost  
 169 in at least one dimension of space–time in order to achieve scale decomposition.  
 170 Processes localized in space and time are thus naturally embedded in (1) and (2).

171 Although the terms in (1) and (2) have the conventional names (e.g., Orlanski and  
 172 Katzfey 1991; Chang 1993), they are actually distinctly different from those in traditional  
 173 formalisms. The most distinct terms are  $\Gamma_A^\varpi$  and  $\Gamma_K^\varpi$ , which are the processes that we are  
 174 most interested in for this study. In appendix A we will see that they both have a *Lie*  
 175 *bracket form, and possess the property of Jacobian identity, reminiscent of the Poisson*  
 176 *bracket in Hamiltonian dynamics; they also satisfy a detailed balance relation. Most*  
 177 *importantly, they sum to zero over scale window  $\varpi$  and location  $n$ .* This conservation  
 178 property, though simple to state, does not hold in previous energetic formalisms. To

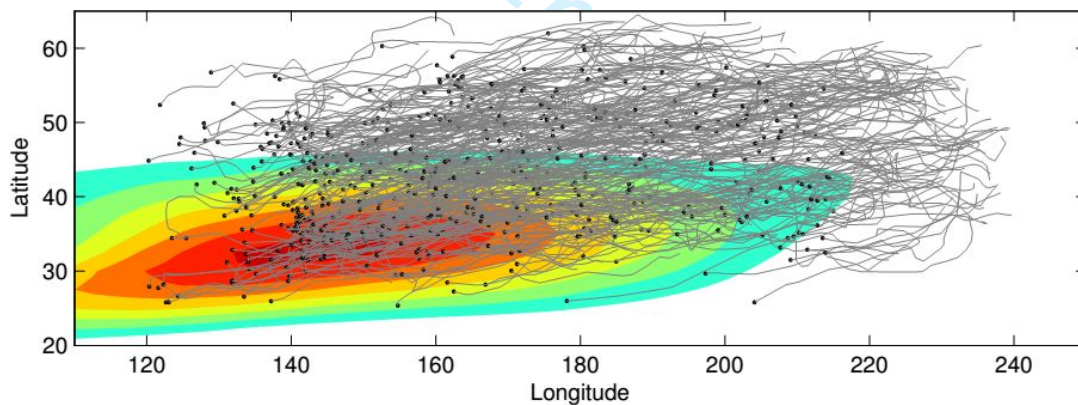
1  
2  
3  
4 179 distinguish it from those that may have been encountered in the literature, the above  
5  
6  
7 180 transfer is termed *canonical transfer*.

8  
9 181 The canonical transfers ( $\Gamma_A^{\varpi}$  and  $\Gamma_K^{\varpi}$ ) in (1) and (2) are very important. Particularly,  
10  
11 182 the mean-to-eddy parts of them (written as  $\Gamma_A^{0 \rightarrow 1}$  and  $\Gamma_K^{0 \rightarrow 1}$ ) correspond to the two  
12  
13  
14 183 important geophysical fluid flow processes, *i.e.*, baroclinic instability and barotropic  
15  
16  
17 184 instability of the mean flow (see Liang and Robinson, 2007), though whether they are  
18  
19  
20 185 equivalent is still in dispute (e.g., Farrell, 1984; 1985; 1989; Plumb, 1983). For  
21  
22 186 mnemonic reason, in the following,  $\Gamma_A^{0 \rightarrow 1}$  and  $\Gamma_K^{0 \rightarrow 1}$  may be referred to as, respectively,  
23  
24  
25 187 baroclinic and barotropic canonical transfers. Conversely, the eddy-to-mean parts, written  
26  
27 188 as  $\Gamma_A^{1 \rightarrow 0}$  and  $\Gamma_K^{1 \rightarrow 0}$ , can be used to investigate the eddy feedback processes. They  
28  
29  
30 189 respectively correspond to the baroclinic and barotropic feedback mechanisms. See  
31  
32  
33 190 Figure A1 for an illustration.

### 35 191 **3.2 Eddy tracking and compositing**

36  
37 192 The methods used in this study also include an eddy tracking and compositing  
38  
39  
40 193 technique. Because of the migration of the eddies and the inhomogeneity of the  
41  
42  
43 194 background flow, an eddy-following approach is needed to investigate the localized  
44  
45  
46 195 interaction. Here the tracking algorithm developed by Hodges (1995) is used to fulfil this  
47  
48  
49 196 task. In practical use, the maxima of the 850-hPa relative vorticity ( $\xi_{850}$ ) are chosen as  
50  
51 197 the indicator of the storm center (or feature point), which forms the nodes of the storm  
52  
53  
54 198 trajectory (Hoskins and Hodges, 2002). Besides, before tracking the vorticity maxima  
55  
56 199 associated with weather storms it is necessary to remove the background field, *i.e.*, the

1  
2  
3  
4 200 slowly varying, large spatial scale part of the field (Anderson et al. 2003). Here, we use  
5  
6  
7 201 the synoptic vorticity reconstructed by the MWT as the indicator. That is to say, the  
8  
9  
10 202 eddies tracked are storms in the synoptic scale window. Following previous studies, the  
11  
12 203 cyclogenesis time is defined as the first time when  $\xi_{850}$  exceeds  $1 \times 10^{-5} \text{ s}^{-1}$ . In this  
13  
14 204 study, we only select the long-lived storms whose  $\xi_{850}$  remains larger than  $1 \times 10^{-5} \text{ s}^{-1}$   
15  
16 205 for at least 4 days after their genesis. Also, only storms with a maximum  $\xi_{850}$  greater  
17  
18 206 than  $5 \times 10^{-5} \text{ s}^{-1}$  are retained for the analysis. Finally, trajectories of 2189 cold-month  
19  
20 207 (from October to April) storms in the North Pacific storm-track area [ $20^\circ\text{N}$ - $70^\circ\text{N}$ ;  
21  
22 208  $120^\circ\text{E}$ - $240^\circ\text{E}$ ] are obtained. A sample of the selected trajectories are displayed in Figure  
23  
24  
25  
26  
27  
28 209 1.



210  
211 **Figure 1.** Sample of storm trajectories based on  $\xi_{850}$ . The gray lines stand for trajectories,  
212 with black dots indicating their respective starting points, and the shaded area for the  
213 climatological wintertime 300-hPa zonal wind, starting from  $20 \text{ m s}^{-1}$  with an interval of  
214  $5 \text{ m s}^{-1}$ .

215 The cyclone trajectories obtained are used for the compositing of the spatial  
216 structures. Considering the large case-to-case variability (Sinclair and Revell, 2000), we

1  
2  
3  
4 217 use the compositing method with a large number of individual storms in order to get a  
5  
6 218 statistical result. A detailed description of the methodology can be found in Bengtsson et  
7  
8  
9 219 al. (2007) for a radial sampling grid since modified for a rectangular sampling grid. In  
10  
11  
12 220 brief, it consists of the following procedures:

13  
14 221 \* First, select the tracks to be used. (In the present study, the storms of interest are  
15  
16  
17 222 the 2189 long-lived strong storms.)

18  
19 223 \* Second, create a rectangular grid centered on the equator with uniform grid  
20  
21  
22 224 spacing and chosen side length (respectively 0.5 and 40 degrees here).

23  
24 225 \* Third, rotate the grid to the storm center and rotate it to align with the direction of  
25  
26  
27 226 the storm propagation, which is determined by the displacement of the storm center using  
28  
29  
30 227 a second-order, central differencing scheme. Using the rotated composite can reduce the  
31  
32  
33 228 impact of the difference in the storm propagation direction on the composite storm  
34  
35  
36 229 structure.

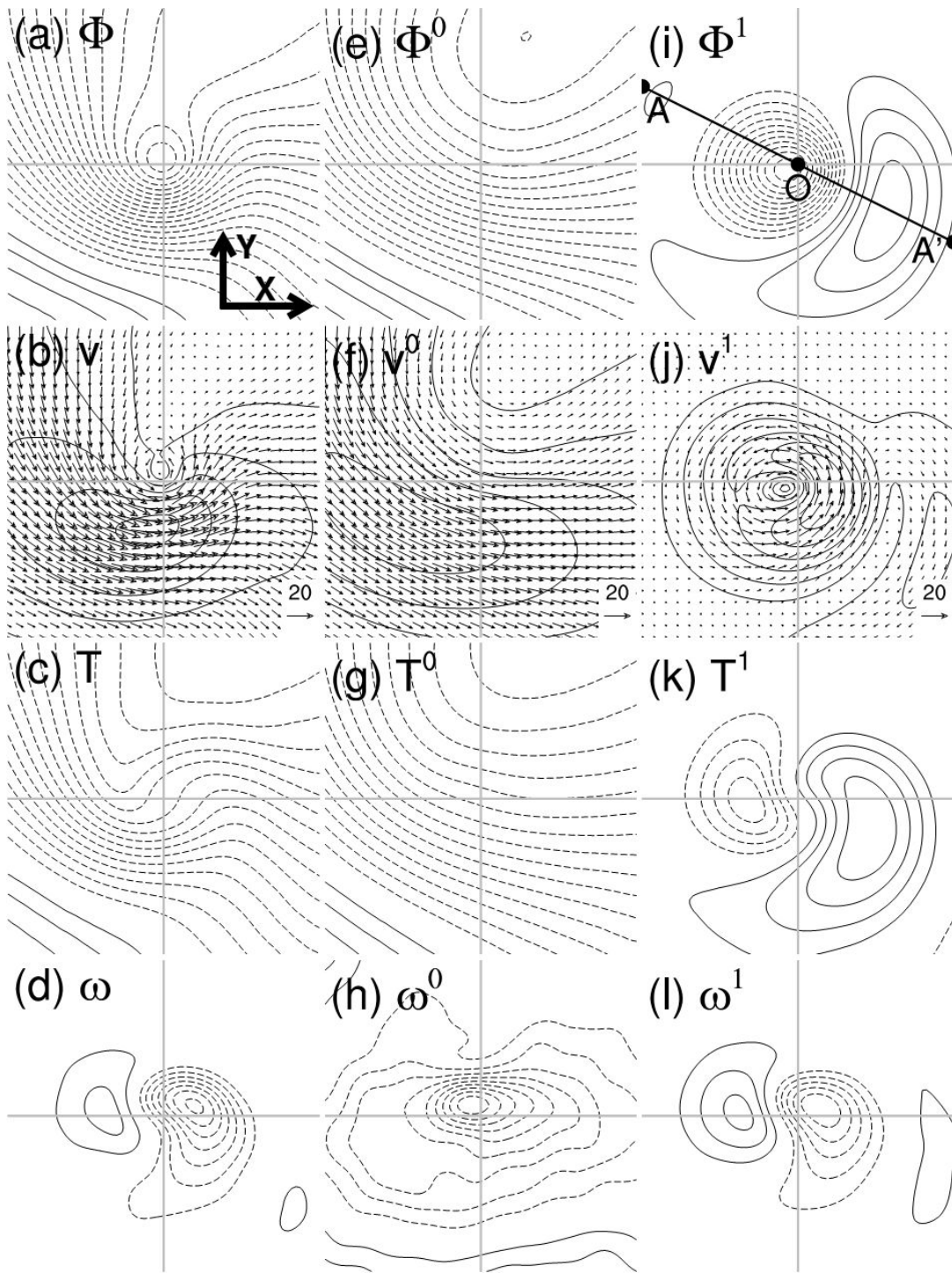
37  
38 230 \* Finally, the required field is sampled on to the rectangular grid, for each storm at  
39  
40  
41 231 each time step along the full lifecycle of the storms and then averaged over the selected  
42  
43  
44 232 storms at selected stages of the lifecycle. For the averaging, we need a reference time for  
45  
46  
47 233 the lifecycle. In this study, the instant of maximal intensity is chosen as  $t = 0$ , and then  
48  
49  
50 234 the time is measured as offset to this reference time. For example, -4 (4) stands for 4 time  
51  
52  
53 235 steps (or 24 h) before (after) the storm reaches its maximal intensity. [In this study, the](#)  
54  
55  
56 236 [standard deviation is used to show the case-to-case variability within the composites.](#)

#### 237 4. MS-EVA setup

238 The analysis begins with a determination of the scale window bounds. In this study,  
239 we need two windows: a synoptic-scale window and a low-frequency background flow  
240 window. According to previous studies, these windows are set to be bounded by a period  
241 of 16 days (in MWT, the number of time steps is required to be a power of 2). We have  
242 also tried 8 days as the window bound and found that the synoptic signal cannot be  
243 completely separated from the total fields. This is essentially the same as Deng and Mak  
244 (2006), who applied a 15-day high-pass filter in their diagnostics. Besides, Anderson et  
245 al. (2003) observed that band-pass filtering with a time period of 2.5-6 days (e.g.,  
246 Blackmon, 1976) may have a detrimental impact on individual weather systems (see also  
247 Chang, 1993), and a 20-day high-pass filter is a good choice.

248





249

250 **Figure 2. Left column:** distributions of the 500-hPa composite original fields at the  
 251 maximal intensity time ( $t=0$ ): (a) geopotential anomalies (contour interval  $200 \text{ m}^2 \text{ s}^{-2}$ ), (b)  
 252 wind vectors ( $\text{m s}^{-1}$ ) and speeds (contour, contour interval  $5 \text{ m s}^{-1}$ ), (c) temperature

1  
2  
3  
4  
5  
6  
7  
8  
9  
10  
11  
12  
13  
14  
15  
16  
17  
18  
19  
20  
21  
22  
23  
24  
25  
26  
27  
28  
29  
30  
31  
32  
33  
34  
35  
36  
37  
38  
39  
40  
41  
42  
43  
44  
45  
46  
47  
48  
49  
50  
51  
52  
53  
54  
55  
56  
57  
58  
59  
60

1  
2  
3  
4 253 anomalies (contour interval 1 K), and (d) vertical velocity (contour interval  $0.04 \text{ Pa s}^{-1}$ ).  
5  
6  
7 254 **Middle column:** same as the left column, but for the background fields, with contour  
8  
9 255 intervals of (e)  $200 \text{ m}^2 \text{ s}^{-2}$ , (f)  $3 \text{ m s}^{-1}$ , (g) 1 K, and (h)  $0.004 \text{ Pa s}^{-1}$ . **Right column:** same  
10  
11 256 as the left column, but for the synoptic fields, with contour intervals of (i)  $100 \text{ m}^2 \text{ s}^{-2}$ , (j)  $2$   
12  
13 257  $\text{m s}^{-1}$ , (k) 0.5 K, and (l)  $0.04 \text{ Pa s}^{-1}$ . Negative contours are dashed and the zero contour is  
14  
15 258 omitted. The composite storm propagates eastward. Each subplot is in a  $40^\circ \times 40^\circ$   
16  
17 259 rectangular grid. The composites are based on the 2185 cold-month (October-April)  
18  
19 260 storms; same below. The corresponding distributions of the standard deviation are given  
20  
21 261 in Figure S3 in the supplementary file.

## 262 5. Composite structure of the original and reconstructed fields

263 In this section, we briefly describe the composite structures of the original and  
264 reconstructed fields. Since the structure of each composite field changes little throughout  
265 the life of the composite storm, only the maps at the storm's maximal intensity time ( $t =$   
266 0) are presented (note that the storm strength changes significantly throughout the life;  
267 see Figures S1 and S2 in the supplementary file). Figure 2 shows the horizontal  
268 distributions of the composite fields at 500 hPa. The side length of each subplot is 40  
269 degrees at the equator (equivalent to 4447 km). The composite system moves from the  
270 left to the right. For convenience, the along-propagation direction will be referred to as  
271 the  $x$ -direction, and the  $y$ -direction and  $z$ -direction are determined through the right-hand  
272 rule, with  $z$  directed upward.

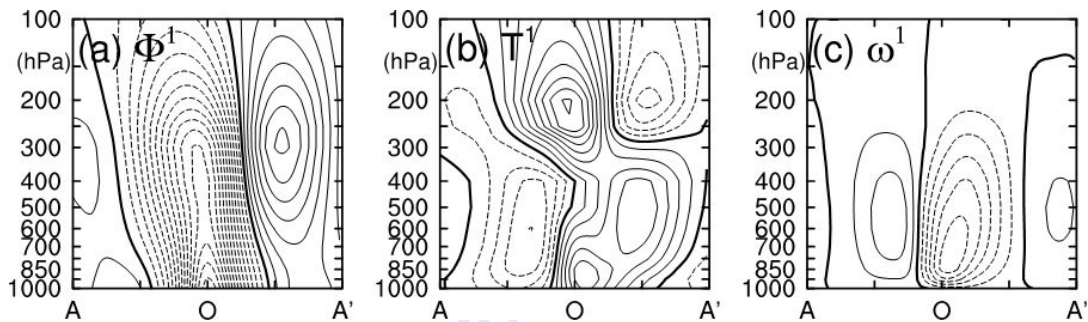
## 273 5.1 The original fields

274 We first look at the original fields. On the map of geopotential anomalies ( $\phi$ ), there  
275 is a trough with closed isopleths (Figure 2a). Correspondingly, a cyclonic circulation  
276 exists on the map of the horizontal wind ( $\mathbf{v}_h$ , Figure 2b). The distribution of the wind  
277 speed is quite inhomogeneous around the storm center, with strong winds occurring in the  
278 south part where the contours of geopotential anomalies are dense. The composite field of  
279 temperature anomalies ( $T$ ) exhibits a wave-like pattern (Figure 2c), with the temperature  
280 trough and ridge located to the west and east of the storm center, respectively. In terms of  
281 the vertical velocity ( $\omega$ ), it shows a dipole pattern (Figure 2d), with upward ( $\omega < 0$ ) and  
282 downward ( $\omega > 0$ ) motions located ahead and behind the geopotential trough,  
283 respectively; the upward motion is much stronger than the downward motion. The  
284 features of these composite fields generally agree with those in previous studies  
285 (Bengtsson et al., 2009; Catto et al., 2010; Dacre et al., 2012; Field and Wood, 2007).

## 286 5.2 The multiscale window reconstructed fields

287 We now look at the composites of the multiscale fields reconstructed by the MWT.  
288 To our knowledge, few studies have explored the storm structure in this way. Figures  
289 2e-2h show the composite maps of the background fields. We see that the contours of  
290 geopotential anomalies ( $\phi^{\sim 0}$ ) are generally northwest-southeastward distributed (Figure  
291 2e), and the closed center appearing in the original field (Figure 2a) has been removed.  
292 The background wind maximum (i.e., the jet stream) is located in the south (Figure 2f).  
293 This is why the maximum wind occurs in the southern part of the storm on the original

294 map (Figure 2b). For temperature anomaly ( $T^{\sim 0}$ ), its distribution (Figure 2g) is similar to  
 295 that of  $\phi^{\sim 0}$ . Regarding  $\omega^{\sim 0}$ , it is negative within almost the whole domain (Figure 2h),  
 296 implying that the storms are generated and evolve within an environment of upward  
 297 motion. The magnitude of  $\omega^{\sim 0}$  is about 10% of the original field (note the difference in  
 298 the contour interval between them).



299 **Figure 3.** Vertical section distributions of the composites of the synoptic fields: (a)  
 300 geopotential anomalies (contour interval  $100 \text{ m}^2 \text{ s}^{-2}$ ), (b) temperature anomalies (contour  
 301 interval  $0.5 \text{ K}$ ), and (c) vertical velocity anomalies (contour interval  $0.04 \text{ Pa s}^{-1}$ ).  
 302 Negative contours are dashed and the zero contour is in bold. All these sections are taken  
 303 along the line ( $AOA'$ ) as indicated in Figure 2i. The corresponding distributions of the  
 304 standard deviation are given in Figure S4 in the supplementary file.

306 Figures 2i-2l show the distributions of the composite synoptic fields, which exhibit  
 307 more local features than the background fields. The composite field of the 500-hPa  $\phi^{\sim 1}$   
 308 shows a low-high pair (Figure 2i). The low anomaly has compact structure and large  
 309 amplitude, accompanying a strong cyclonic circulation (Figure 2j), whereas its  
 310 counterpart is broad and weak. For the other anomaly fields ( $T^{\sim 1}$  and  $\omega^{\sim 1}$ ), generally  
 311 show a dipolar pattern (Figures 2k and 2l). Their distributions are configured in the way

1  
2  
3  
4 312 that the moist-warm air ascends in the front part of the storm and the dry-cold air  
5  
6 313 subsides in the rear part.  
7  
8

9 314 The vertical structure of the composite synoptic system is also examined. Figure 3  
10  
11 315 shows the distributions of the composite synoptic fields along the section  $AOA'$  as  
12  
13  
14 316 indicated in Figure 2i. This generally exhibits the structure of typical midlatitude  
15  
16 317 baroclinic waves, with a zonal wavelength of  $\sim 4000$  km and a westward (eastward) tilting  
17  
18 318 of the phase line of  $\phi^{\sim 1}$  ( $T^{\sim 1}$ ) with altitude (Chang, 1993; Hartmann, 1974; Lau, 1979;  
19  
20 319 Lim and Wallace, 1991). However, note the strong cyclone-anticyclone asymmetry. For  
21  
22 320 example, the cyclone is strongest at low levels, whereas the accompanying anticyclone  
23  
24 321 achieves its maximum at upper levels with weak signal at the earth surface (Figure 3a).<sup>1</sup>  
25  
26 322 For  $\omega^{\sim 1}$ , the upward motion in the front part is much stronger than the downward motion  
27  
28 323 in the rear (Figure 3c).  
29  
30  
31  
32  
33  
34

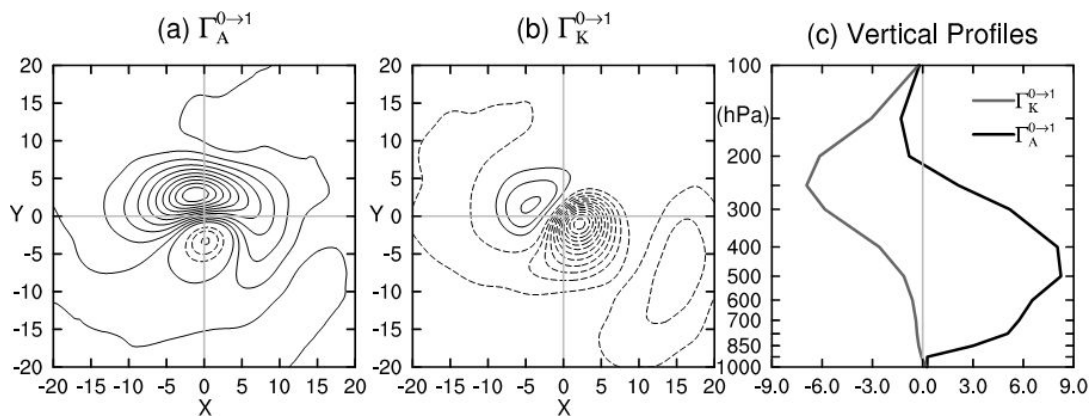
## 35 324 **6. Nonlinear eddy-mean flow interaction**

### 36 325 **6.1 Spatial structure of the canonical transfers**

37  
38 326 The eddy-mean flow interaction includes the canonical transfer from the mean flow  
39  
40  
41 327 to the eddies ( $\Gamma_A^{0 \rightarrow 1}$  and  $\Gamma_K^{0 \rightarrow 1}$ ) and for the opposite direction ( $\Gamma_A^{1 \rightarrow 0}$  and  $\Gamma_K^{1 \rightarrow 0}$ ). The  
42  
43 328 former is a quantitative description of the mean-to-eddy transfer and the latter  
44  
45 329 characterizes the eddy feedback. We first look at the spatial structure of the former.  
46  
47  
48  
49  
50  
51  
52  
53

---

54  
55 <sup>1</sup> To the best of our knowledge, the splitting of the warm center (at 850 hPa) ahead of the cyclone has  
56 not been observed (Figure 3b).  
57  
58  
59  
60



330

331 **Figure 4.** Horizontal distributions of the vertically integrated (from 1000 hPa to 100 hPa)332 (a)  $\Gamma_A^{0 \rightarrow 1}$  and (b)  $\Gamma_K^{0 \rightarrow 1}$  at the maximal intensity time ( $t=0$ ), with a contour interval of333  $2 \times 10^{-4} \text{ m}^2 \text{ s}^{-3}$ ; and (c) the vertical distributions of  $\Gamma_A^{0 \rightarrow 1}$  and  $\Gamma_K^{0 \rightarrow 1}$  ( $10^{-4} \text{ m}^2 \text{ s}^{-3}$ )

334 averaged over the storm area. The corresponding distributions of the standard deviation

335 are given in Figure S5 in the supplementary file.

336 Figure 4 shows the horizontal distributions of the vertically integrated (from 1000

337 hPa to 100 hPa)  $\Gamma_A^{0 \rightarrow 1}$  and  $\Gamma_K^{0 \rightarrow 1}$ . Figure 4a shows a dipolar pattern for the  $\Gamma_A^{0 \rightarrow 1}$ , with a

338 strong positive center in the north of the storm and a weak negative center in the south.

339 This means that the background flow experiences a downscale canonical APE transfer in

340 the north of the storm, while an upscale canonical APE transfer in the southern region.

341 The barotropic canonical transfer  $\Gamma_K^{0 \rightarrow 1}$  (Figure 4b), also exhibits a dipolar distribution

342 within the storm area, with a negative region at the front and a positive one at the rear,

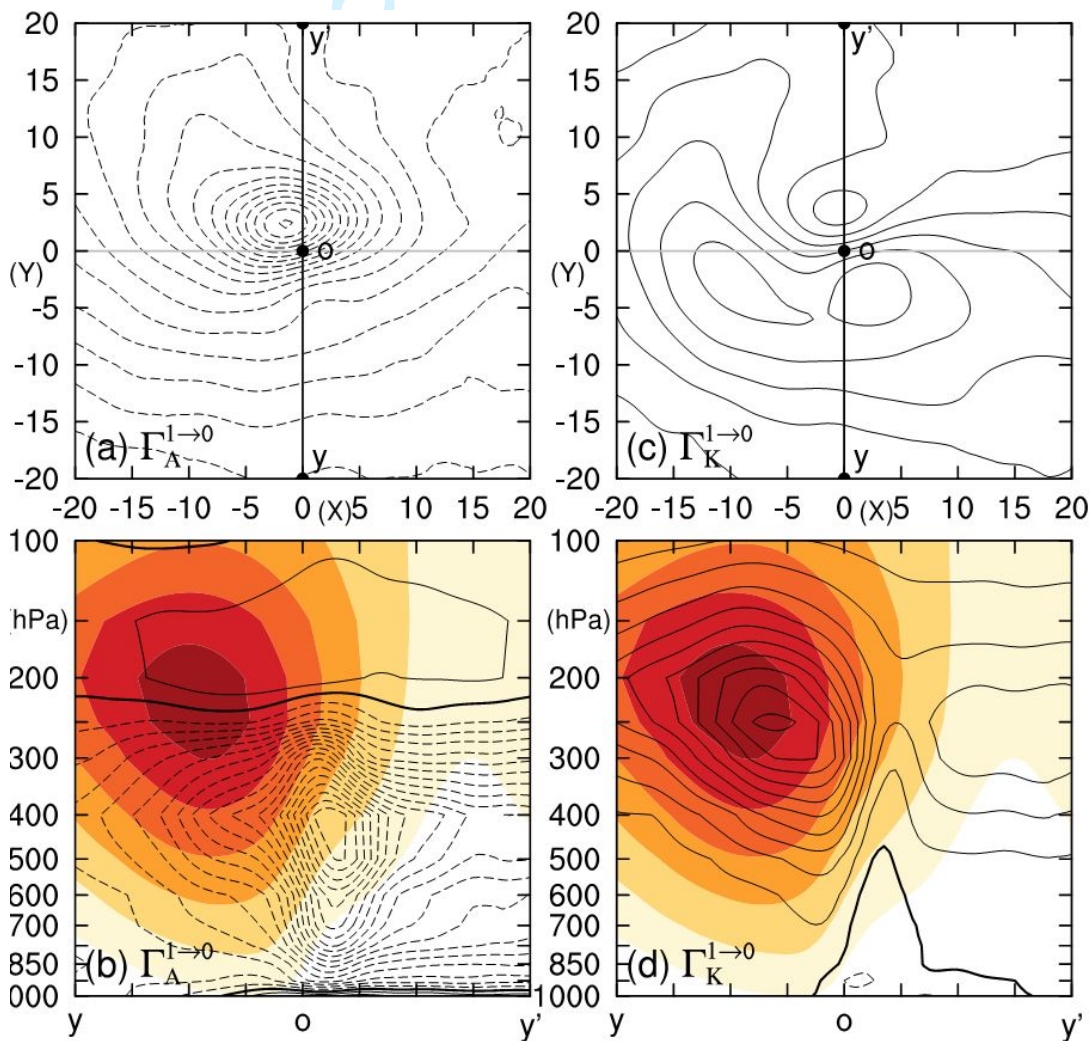
343 implying upscale and downscale canonical KE transfers in the respective regions. In

344 terms of the amplitude the negative barotropic canonical transfer center is stronger than

345 its positive counterpart. On the whole, the storm has a favorable configuration for APE to

346 be transferred from the mean flow, and for KE to be transferred to the mean flow,

347 consistent with the traditional perspective (Barnes and Young, 1992; Orlandi and Chang,  
 348 1993; Simmons and Hoskins, 1978, 1980). Figure 4c shows the vertical profiles of  $\Gamma_A^{0 \rightarrow 1}$   
 349 and  $\Gamma_K^{0 \rightarrow 1}$  averaged horizontally over the storm area. We see that  $\Gamma_A^{0 \rightarrow 1}$  is positive  
 350 almost throughout the entire troposphere. The maximum center occurs at 400 hPa. In  
 351 contrast,  $\Gamma_K^{0 \rightarrow 1}$  is negative through the whole depth, implying the kinetic energy transfer  
 352 is from the storm to the background flow. It is strong at upper levels and reaches its  
 353 maximum magnitude at 250 hPa.

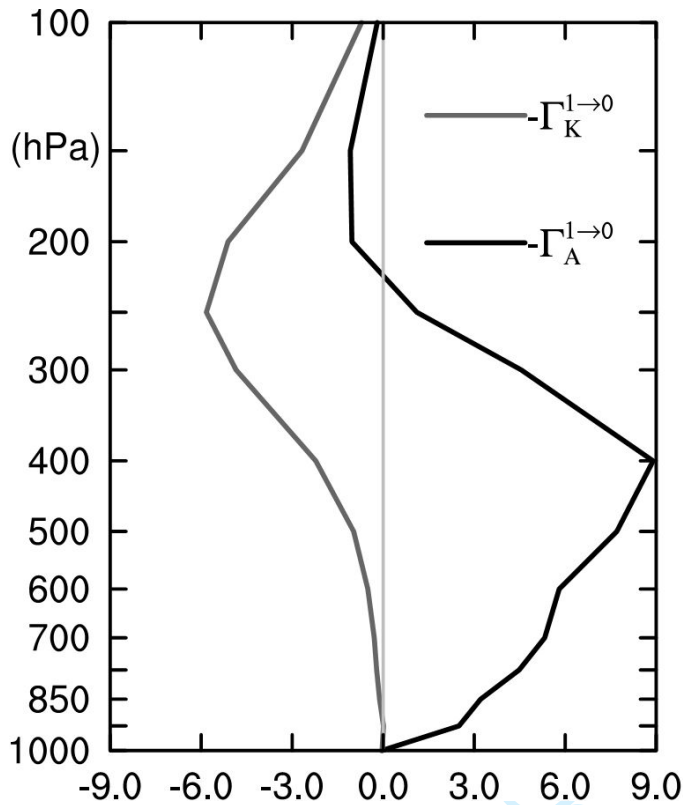


354  
 355 **Figure 5.** Spatial distributions of  $\Gamma_A^{1 \rightarrow 0}$  and  $\Gamma_K^{1 \rightarrow 0}$  at the maximal intensity time (t=0):

1  
2  
3  
4 356 the vertically averaged (a)  $\Gamma_A^{1 \rightarrow 0}$  and (c)  $\Gamma_K^{1 \rightarrow 0}$ ; the sectional distributions of (b)  $\Gamma_A^{1 \rightarrow 0}$   
5  
6  
7 357 and (d)  $\Gamma_K^{1 \rightarrow 0}$  along the line  $yoy'$  as indicated in (a) and (c). The contour interval is  
8  
9 358  $0.5 \times 10^{-4} \text{ m}^2 \text{ s}^{-3}$ . In (b) and (d), overlaid is the background wind speed  $|\mathbf{v}^{\sim 0}|$  (shaded;  
10  
11 359 contour interval  $4 \text{ m s}^{-1}$ ). The corresponding distributions of the standard deviation are  
12  
13  
14 360 given in Figure S6 in the supplementary file.

15  
16  
17 361 The spatial distributions of the eddy feedback, characterized by  $\Gamma_A^{1 \rightarrow 0}$  and  $\Gamma_K^{1 \rightarrow 0}$ , are  
18  
19 362 shown in Figure 5. We see that horizontally  $\Gamma_A^{1 \rightarrow 0}$  is negative within the entire domain  
20  
21  
22 363 (Figure 5a), implying a downscale canonical APE transfer. But, the transfer is  
23  
24 364 inhomogenous within the composite storm, with strong energy transfer mainly confined  
25  
26  
27 365 in the northern area. Vertically,  $\Gamma_A^{1 \rightarrow 0}$  is negative through almost the entire troposphere  
28  
29  
30 366 (Figure 5b). The peak occurs at 400 hPa and on the northern flank of the jet (also the  
31  
32 367 storm center). In short, the spatial distribution of  $\Gamma_A^{1 \rightarrow 0}$  is similar to that of  $\Gamma_A^{0 \rightarrow 1}$ . For  
33  
34  
35 368  $\Gamma_K^{1 \rightarrow 0}$ , it is generally positive (Figure 5c), implying an upscale KE canonical transfer. Note  
36  
37  
38 369 that this upscale transfer is significant at upper levels, especially at the jet core (Figure  
39  
40 370 5d). Figure 6 gives the vertical profiles of  $\Gamma_A^{1 \rightarrow 0}$  and  $\Gamma_A^{1 \rightarrow 0}$ . It can be seen that their  
41  
42  
43 371 distributions are almost the same as the mean-to-eddy counterparts (Figure 4c), but with  
44  
45  
46 372 the opposite sign.





373  
374 Figure 6. The vertical distributions of  $-\Gamma_A^{1 \rightarrow 0}$  and  $-\Gamma_K^{1 \rightarrow 0}$  ( $10^{-4} \text{ m}^2 \text{ s}^{-3}$ ) averaged over  
375 the storm area.

## 376 6.2 Time evolution

377 The nonlinear eddy-mean flow interaction is not steady. Here, we are more  
378 interested in how the eddy-feedback process evolves where there is a storm passing  
379 through. To show this for a particular storm, we first identify the central location of the  
380 storm at its maximum intensity time ( $t=0$ ), and then sample the vertical cross section of  
381 the fields (here  $\Gamma_A^{1 \rightarrow 0}$  and  $\Gamma_K^{1 \rightarrow 0}$ ) at that location meridionally at each time step from -12  
382 to 12 (corresponding to from day -3 to day 3)<sup>1</sup>. In sampling, the fields at each time step

<sup>1</sup> Here we choose a duration of 6 days, considering that the mean life cycle of the 2189 storms lasts  $5.37 (\pm 0.03)$  days.

are also rotated with respect to the storm propagation direction at  $t=0$ . Following this way, we can get the latitude-time section of any field at a particular location as a storm approaches, passes, and recedes<sup>1</sup>. This procedure is applied to each of the 2189 selected storms. Finally, the obtained sections are averaged over all the samples at each time step.

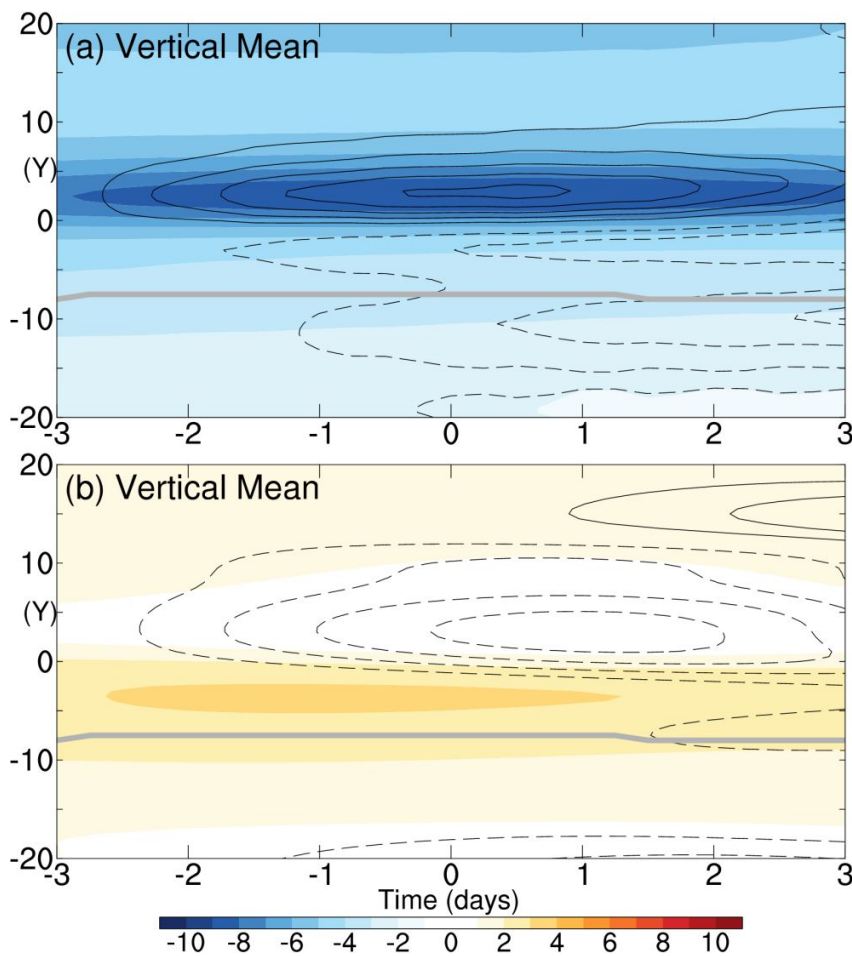


**Figure 7.** Vertically averaged latitude-time sections of the composite  $\Gamma_A^{1\rightarrow 0}$  (a;  $10^{-4} \text{ m}^2 \text{ s}^{-3}$ ) and  $\Gamma_K^{1\rightarrow 0}$  (b;  $10^{-4} \text{ m}^2 \text{ s}^{-3}$ ). The contours show the changes in magnitude relative to the initial state (at day -3), which are calculated as  $A' = |A| - |A_*|$ , with  $A$  the original

<sup>1</sup> Here we switch to the Eulerian approach in order to obtain the spatio-temporal distribution of the interaction and, particularly, the background flow response (see below).

1  
2  
3  
4 391 field and  $A_*$  the field at day -3<sup>1</sup>. The contour interval is  $0.2 \times 10^{-4} \text{ m}^{-2} \text{ s}^{-3}$ . The thick  
5  
6  
7 392 gray curve in (a) and (b) denotes the latitude where the 300-hPa background wind is  
8  
9 393 maximized (i.e., jet axis). The corresponding distributions of the standard deviation are  
10  
11  
12 394 given in Figure S7 in the supplementary file.

13  
14 395 Figure 7 shows the general time evolution of  $\Gamma_A^{1 \rightarrow 0}$  and  $\Gamma_K^{1 \rightarrow 0}$ . We see that as the  
15  
16  
17 396 storm passes, the downscale APE transfer is intensified within a narrow zonal band north  
18  
19  
20 397 of the storm center, whereas elsewhere it is slightly weakened (Figure 7a). In contrast, the  
21  
22  
23 398 upscale KE transfer is intensified slightly within a narrow zonal band on the southern  
24  
25  
26 399 side, while in the north it is greatly weakened (Figure 7b). The changes of  $\Gamma_A^{1 \rightarrow 0}$  and  
27  
28  
29 400  $\Gamma_K^{1 \rightarrow 0}$  begin from about 3 days before the storm arrives, achieve their maxima as the  
30  
31  
32 401 storm arrives, and then weaken. In the presence of the storm,  $\Gamma_A^{1 \rightarrow 0}$  and  $\Gamma_K^{1 \rightarrow 0}$  seem to  
33  
34  
35 402 take place complementarily in the horizontal plane:  $\Gamma_K^{1 \rightarrow 0}$  intensifies (weakens) wherever  
36  
37  
38 403  $\Gamma_A^{1 \rightarrow 0}$  substantially weakens (intensifies).

39  
40 404 The most interesting finding in this section is the spatial asymmetry of the  
41  
42  
43 405 eddy-mean flow interaction: the downscale canonical APE transfer process mainly  
44  
45  
46 406 happens in the northern part of the storm (also on the northern flank of the jet stream) and  
47  
48  
49 407 in middle levels, whereas the upscale canonical KE transfer mainly occurs in the south,  
50  
51  
52 408 overlaid with the jet core. The former acts to destroy the background baroclinicity,  
53  
54  
55 409 whereas the latter acts to accelerate the jet and thus enhance the baroclinicity. These

---

55  
56 <sup>1</sup> Here we want to see the change in energy transfer as a storm arrives but initially there is no storm, so  
57 we choose an earlier day (i.e., day -3) rather than day 0.

1  
2  
3  
4 410 competing effects essentially determine the final state of the jet stream after the storm  
5  
6  
7 411 passes. We will elaborate on this in the following section.  
8

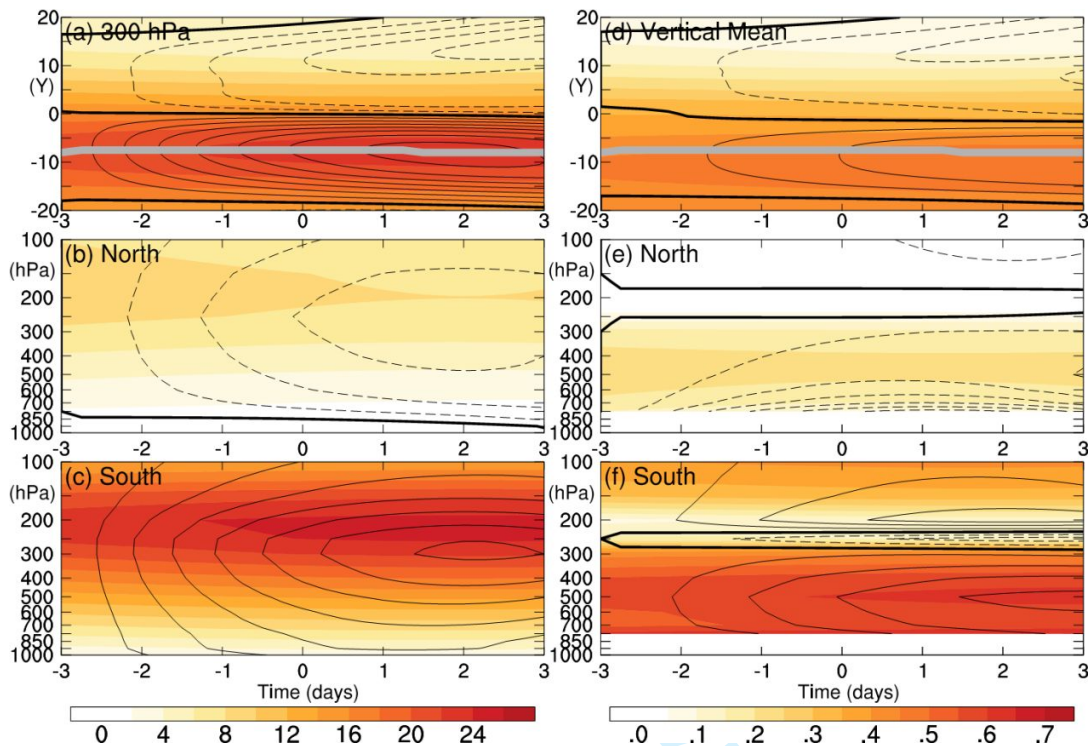
## 9 412 **7. Response of the background flow and baroclinicity**

10  
11 413 In this study, we focus on the responses of the background wind and baroclinicity.  
12  
13  
14 414 Figure 8 shows the composite sections of the background wind (left column). We see that  
15  
16  
17 415 as the storm passes, the wind decreases in the north, whereas it increases in the south,  
18  
19  
20 416 showing an anomalous dipolar pattern (Figure 8a). Moreover, the increase in the south is  
21  
22  
23 417 stronger than the decrease in the north. Since the jet core is located in the south of the  
24  
25 418 storm (cf. Figure 3), this tends to strengthen and narrow the jet (by 2 latitudes)<sup>1</sup>. Figures  
26  
27 419 8c and 8d show the composite pressure-time sections of the background wind along the  
28  
29  
30 420 latitudes of 10° and -10°, respectively. It can be seen that either in the north or in the  
31  
32  
33 421 south, the response of the background wind is more significant in the upper troposphere  
34  
35 422 (Figures 8b and 8c). Temporally, the background wind begins to change from about 3  
36  
37 423 days before the storm's arrival, and responds strongly as the storm arrives. A closer  
38  
39  
40 424 observation reveals that the largest change occurs at  $t=2d$  instead of  $t=0$  (see also the  
41  
42  
43 425 energy transfers in Figure 7). This may be due to the consecutive influence of secondary  
44  
45  
46 426 cyclones formed along the trailing cold front of the reference one (e.g., Papritz and  
47  
48 427 Schemm 2013). Overall, the jet does not show any obvious meridional shift. This is  
49  
50  
51 428 consistent with the argument of Vallis and Gerber (2008) that, if the storm is generated  
52  
53

---

54  
55  
56 <sup>1</sup> This estimation is based on the half jet-width, which is measured by the distance between the latitude of maximum  
57 wind and the northward latitude at which the wind reaches half of its peak.

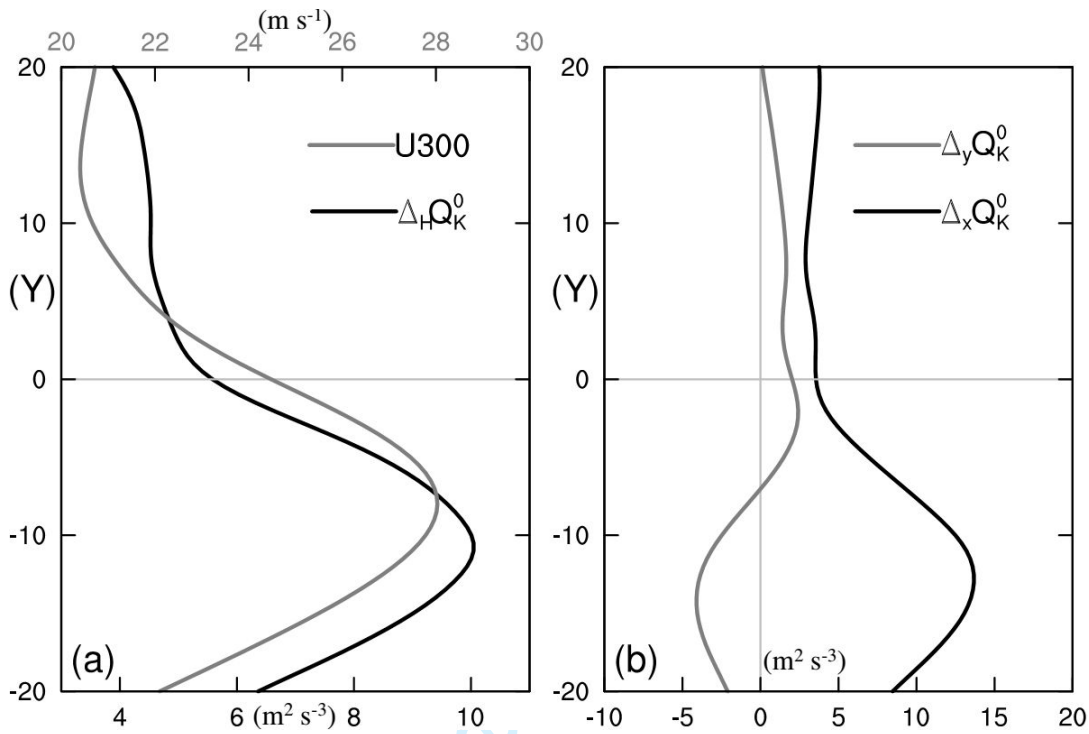
429 on the flank of the jet, the storm would act to maintain the jet's latitude. For the  
 430 background wind response at any instant (e.g.,  $t=0$ ), the meridional structure is similar to  
 431 that obtained by Chang (2001b) using wave packet regression.



432  
 433 **Figure 8.** Left column: same as Figure 7, but for the background wind speed (shaded,  $\text{m s}^{-1}$ ) and its anomaly (contoured, with an interval of  $0.25 \text{ m s}^{-1}$ ); (a) shows the  
 434 latitude-time section at 300 hPa; (b) and (c) show the pressure-time sections along the  
 435 latitudes of  $10^\circ$  and  $-10^\circ$ , respectively. The thick gray curve in (a) and (d) denotes the  
 436 latitude of the maximum of the 300-hPa background wind. Right column: same as the left  
 437 column, but for the baroclinicity, i.e., the Eady growth rate (shaded; in  $\text{day}^{-1}$ ) and its  
 438 anomaly (contoured, with an interval of  $0.01 \text{ day}^{-1}$ ). The corresponding distributions of  
 439 the standard deviation are given in Figure S8 in the supplementary file.

1  
2  
3  
4 441 The latitude-time section of the baroclinicity, measured by  $fN^{-1}|\partial\bar{v}/\partial z|$  (where  $N$   
5  
6  
7 442 is the static stability and other symbols are conventional), is also shown in Figure 8 (right  
8  
9 443 column). We see that, as the storm passes, the baroclinicity weakens in the north, whereas  
10  
11  
12 444 it strengthens in the south (Figure 8d). Vertically, the largest northern weakening happens  
13  
14  
15 445 in the lower troposphere (Figure 8e), while the strongest southern strengthening occurs at  
16  
17 446 middle levels (Figure 8f).

18  
19  
20 447 There is a discrepancy between the evolution of the energy transfers and that of the  
21  
22 448 background flow. Figure 7 suggests that the downscale transfer north of the cyclone is  
23  
24  
25 449 much stronger than the upscale transfer south of the cyclone, while Figure 8 show that the  
26  
27  
28 450 jet/baroclinicity decrease north of the cyclone is somewhat smaller than the jet/baroclinic  
29  
30  
31 451 increase south of the cyclone. How does this discrepancy happen? In fact, the energy  
32  
33 452 transfer is not the only factor that can cause change in the background field. In addition to  
34  
35  
36 453 the nonlinear interaction process, many other energy processes (e.g., energy flux  
37  
38  
39 454 convergences) are also involved, and they can redistribute the energy in horizontal space  
40  
41  
42 455 (Papritz and Schemm 2013; Rivière et al. 2015). Figure 9 shows the mean distribution of  
43  
44  
45 456 the horizontal kinetic energy flux convergence along the meridional direction. It can be  
46  
47  
48 457 seen that the convergence is strong on the southern side of the storm center and peaks  
49  
50  
51 458 near the jet center. Moreover, the convergence is mainly due to the zonal component of  
52  
53  
54 459 the KE flux (Figure 9b). This indicates that, apart from the energy transfer, nonlocal  
55  
56  
57 460 processes also play a role in the enhancement of the background flow in the southern side  
58  
59  
60 461 of the storm.



462

463 **Figure 9.** (a) Mean distributions of the horizontal kinetic energy flux convergence (in  
 464 black; 10<sup>-4</sup> m<sup>2</sup> s<sup>-3</sup>) and 300-hPa wind speed (in gray; m s<sup>-1</sup>) versus y; (b) same as (a), but  
 465 for the x- and y-components of the kinetic energy flux convergence.

466 **8. Discussion**

467 In the above we have discussed about the average results of all the 2189 storms, and  
 468 overall the composite storm is located on the northern side of the maximum background  
 469 wind speed (refer to Figures 2, 5, etc.). But if we have a closer look at these storms,  
 470 actually four types of relative locations can be classified.

471 In order to determine the relative location of a storm, we sample the 300-hPa zonal  
 472 wind in equal-distance along the meridian passing through the storm center. We take the  
 473 center as the starting point (0°) and sample the wind speed once every 2.5° to the south  
 474 and north, respectively. The sampling range is from -20° (south) to 20° (north). Based on

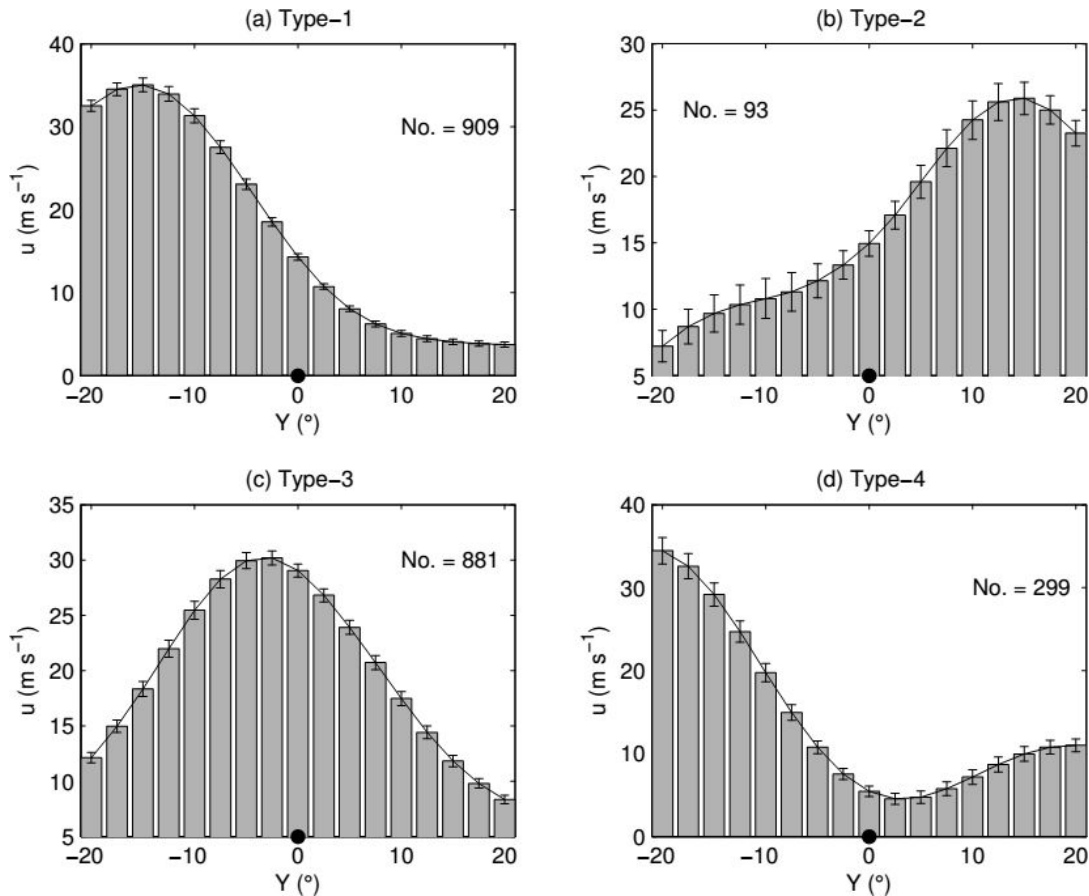
1  
2  
3  
4  
5  
6  
7  
8  
9  
10  
11  
12  
13  
14  
15  
16  
17  
18  
19  
20  
21  
22  
23  
24  
25  
26  
27  
28  
29  
30  
31  
32  
33  
34  
35  
36  
37  
38  
39  
40  
41  
42  
43  
44  
45  
46  
47  
48  
49  
50  
51  
52  
53  
54  
55  
56  
57  
58  
59  
60

1  
2  
3  
4 475 the resulting meridional profile of the background zonal wind, the relative location is then  
5  
6  
7 476 determined. We first calculate the average meridional gradient of zonal wind north and  
8  
9  
10 477 south of the storm center, which here is simply represented by the difference  $\Delta =$   
11  
12 478  $\overline{u_{i+1}} - \overline{u_i}$  (the overbar stands for meridional average). For convenience, the average  
13  
14 479 gradient on the southern side and the northern side are referred to as  $\Delta_S$  and  $\Delta_N$ ,  
15  
16  
17 480 respectively. If  $\Delta_S < 0$  and  $\Delta_N < 0$ , it means that the storm center is located on the  
18  
19  
20 481 northern side of the jet, and we call this type of configuration Type-1; if  $\Delta_S > 0$  and  $\Delta_N$   
21  
22 482  $> 0$ , the storm center is located on the southern side of the jet, and we call this  
23  
24  
25 483 configuration Type-2; if  $\Delta_S > 0$  and  $\Delta_N < 0$ , the storm is at the center of the jet, and the  
26  
27  
28 484 configuration is classified as Type-3; if  $\Delta_S < 0$  and  $\Delta_N > 0$ , it means that there are two  
29  
30 485 jets, and the storm lies in between---we call this configuration Type-4.

31  
32  
33 486 By the above classification it is found that there are 909 Type-1, 93 Type-2, 881  
34  
35  
36 487 Type-3, and 299 Type-4 configurations, plus 7 cases belonging to nowhere. The mean  
37  
38  
39 488 meridional profiles of the background zonal wind corresponding to these four  
40  
41  
42 489 configuration types are shown in Figure 10. It can be seen that if only the configuration  
43  
44  
45 490 between the storm and the major jet is considered, the Type-4 case is similar to the  
46  
47  
48 491 Type-1 case, i.e., the configuration with storms located on the northern side of the major  
49  
50  
51 492 jet. The result is, the Type-1 and the Type-4 storms together account for 55.2% of the  
52  
53  
54 493 total 2189 storms, consistent with the previous observation that the storm track is  
55  
56  
57 494 generally located on the poleward flank of the jet (e.g., Blackmon et al., 1977; Chang et  
58  
59  
60 495 al., 2002). On the other hand, the Type-3 storms are not exactly located at the center of



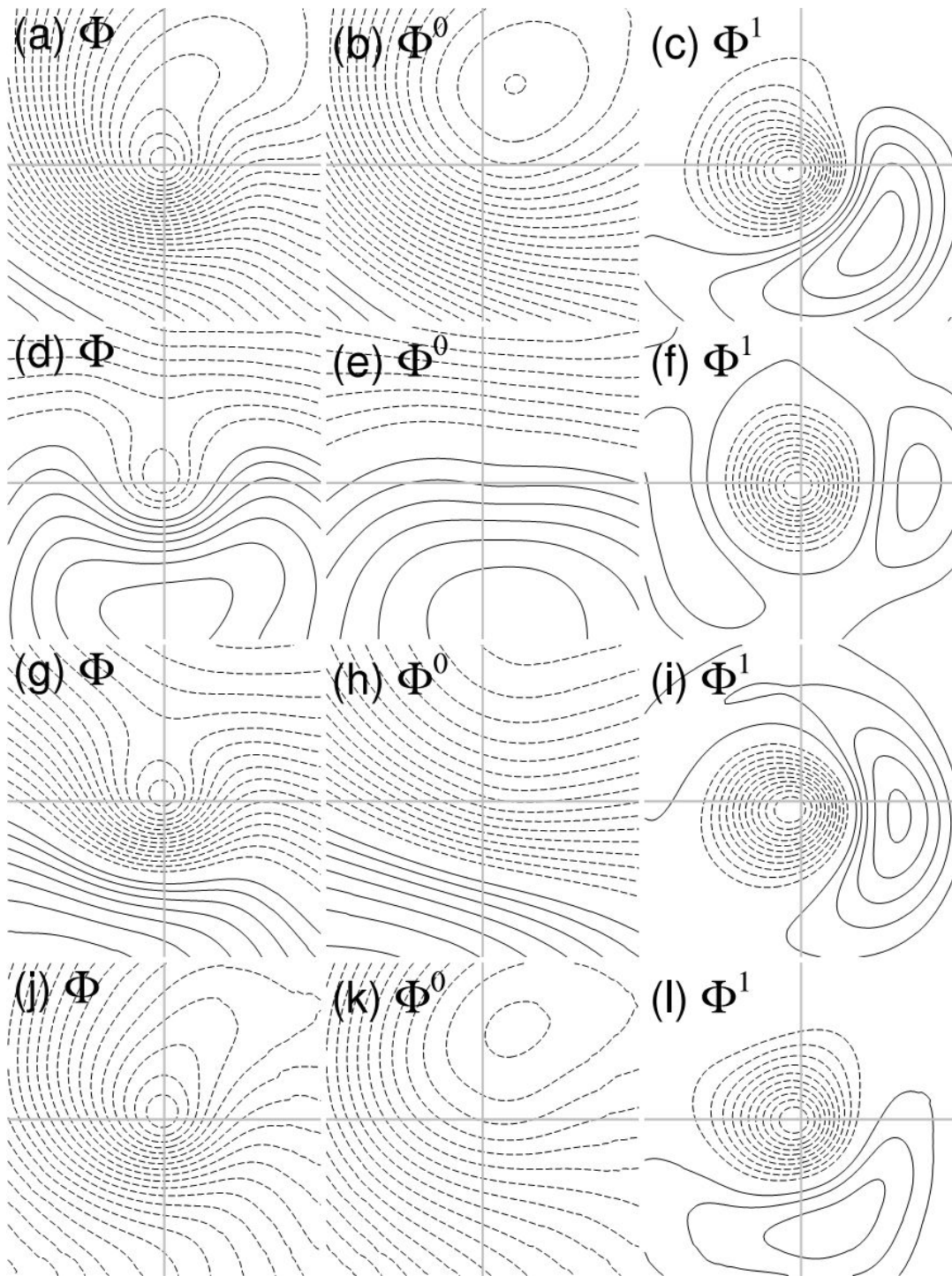
496 the jet, but northward of it by 2.5°. Despite being a minority, 93 storms appear southern  
 497 side of the jet. One may wonder whether these four kinds of storms have different  
 498 interaction scenarios from each other. In the following, we discuss these four types of  
 499 storms separately and compare and contrast them.



500  
 501 Figure 10. The four types of zonal wind profiles. (a) Type-1: the storm is on the northern  
 502 side of the jet; (b) Type-2: the storm is on the southern side of the jet; (c) Type-3: the  
 503 storm is at the jet center; and (d) Type-4: the storm is located between two jets. The black  
 504 dot indicates the meridional location of the storm center. The error bars represent the  
 505 uncertainties of the mean at the 5% significance level.

506 Figure 11 shows the distribution of the composite 500-hPa geopotential anomalies

1  
2  
3  
4 507 for the four types of storms. As expected, the distributions of the Type-1 and Type-4  
5  
6  
7 508 storms are similar since both of them are located on the northern flank of the jet. Besides,  
8  
9 509 their distributions (Figures 11a-c, 11j-l) are similar to the general results as shown in  
10  
11 510 Figures 2a, 2e, and 2i, with a wide trough in the background field (Figures 11b, k) and a  
12  
13  
14 511 dipole in the synoptic field (Figures 11c, l). This is easy to understand because these two  
15  
16  
17 512 types together account for the largest proportion of the total storms. Although the Type-3  
18  
19  
20 513 storm is located near the jet center, the distribution of its geopotential anomalies (Figures  
21  
22 514 11g-i) is still similar to those of Type 1 and Type 4. The obvious difference lies in the  
23  
24  
25 515 Type-2 storm. There is a distinct anti-cyclonic circulation on the southern side of the  
26  
27  
28 516 storm in the original field (Figure 11d), which is not seen in the other three types. In  
29  
30  
31 517 addition, it can be found that the propagation direction of the Type-2 storm is basically  
32  
33 518 parallel to the isolines of the background geopotential (Figure 11e), whereas that of the  
34  
35  
36 519 other three types intersects the isolines and points to the left side.  
37  
38  
39  
40  
41  
42  
43  
44  
45  
46  
47  
48  
49  
50  
51  
52  
53  
54  
55  
56  
57  
58  
59  
60

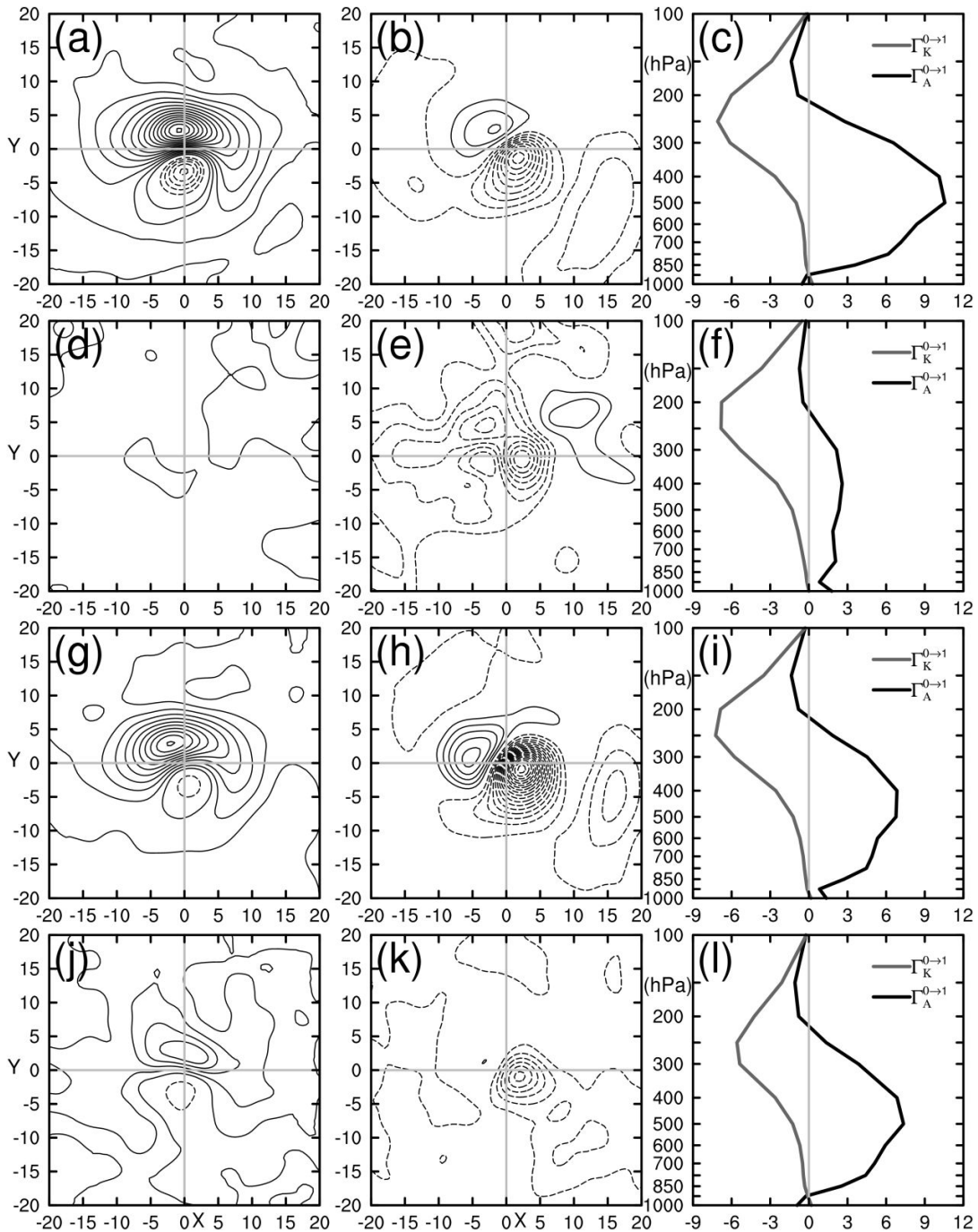


520

521 Figure 11. Same as Figures 2a, 2e, and 2i, but for the Type-1 storm (a, b, c), Type-2  
 522 storm (d, e, f), Type-3 storm (g, h, i), and Type-4 storm (j, k, l), respectively. The  
 523 corresponding distributions of the standard deviations are displayed in Figure S9 in the

1  
2  
3  
4  
5  
6  
7  
8  
9  
10  
11  
12  
13  
14  
15  
16  
17  
18  
19  
20  
21  
22  
23  
24  
25  
26  
27  
28  
29  
30  
31  
32  
33  
34  
35  
36  
37  
38  
39  
40  
41  
42  
43  
44  
45  
46  
47  
48  
49  
50  
51  
52  
53  
54  
55  
56  
57  
58  
59  
60

524 supplementary file.



525  
 526 Figure 12. Same as Figure 4, but for the Type-1 storm (a, b, c), Type-2 storm (d, e, f),  
 527 Type-3 storm (g, h, i), and Type-4 storm (j, k, l), respectively. Left column:  $\Gamma_A^{0 \to 1}$ ;  
 528 Middle column:  $\Gamma_K^{0 \to 1}$ . The corresponding distributions of the standard deviations are

1  
2  
3  
4 529 given in Figure S10 in the supplementary file.  
5  
6  
7

8  
9  
10 530  
11

12 531 The horizontal distributions of the vertically integrated canonical transfers  $\Gamma_A^{0 \rightarrow 1}$   
13 and  $\Gamma_K^{0 \rightarrow 1}$  are given in Figure 12. It can be seen that the Type-1 (Figures 12a, b), Type-3  
14 (Figures 12g, h), and Type-4 (Figures 12j, k) storms generally bear the same structure,  
15 similar to the general results as shown in Figure 4. For instance,  $\Gamma_A^{0 \rightarrow 1}$  shows a dipolar  
16 pattern, with a strong positive center in the north of the storm and a weak negative center  
17 in the south.  $\Gamma_K^{0 \rightarrow 1}$  also exhibits a dipolar distribution within the storm area, with a  
18 negative center at the front and a positive one in the rear (note the positive  $\Gamma_K^{0 \rightarrow 1}$  center  
19 in the Type-4 storm is not obvious). In contrast, the Type-2 storm is quite different.  
20 Horizontally,  $\Gamma_A^{0 \rightarrow 1}$  is mainly distributed in the northeast corner with small values  
21 (Figure 12d), and there is no dipole pattern as observed in the other three types.  $\Gamma_K^{0 \rightarrow 1}$   
22 does not show the dipolar structure, either (Figure 12e); it is negative throughout the  
23 domain, with two minima around the storm center.  
24  
25  
26  
27  
28  
29  
30  
31  
32  
33  
34  
35  
36  
37  
38  
39  
40  
41  
42  
43  
44  
45  
46  
47  
48  
49  
50  
51  
52  
53  
54  
55  
56  
57  
58  
59  
60

40 543 Also presented in Figure 12 are the average vertical distributions of  $\Gamma_A^{0 \rightarrow 1}$  and  
41  $\Gamma_K^{0 \rightarrow 1}$ . The Type-1 (Figure 12c), Type-3 (Figure 12i) and Type-4 (Figure 12l) storms have  
42 the largest amplitude of  $\Gamma_A^{0 \rightarrow 1}$  ( $\Gamma_K^{0 \rightarrow 1}$ ) at middle (high) levels, similar to the general  
43 results previously revealed in Figure 4c. For the Type-2 storm, its  $\Gamma_K^{0 \rightarrow 1}$  profile is also  
44 similar, but its  $\Gamma_A^{0 \rightarrow 1}$  profile is quite different. Although it is still positive through most  
45 of the troposphere, it is quite weak; refer to Table 1 for a quantitative comparison.  
46  
47  
48  
49  
50  
51  
52  
53  
54  
55  
56  
57  
58  
59  
60

549

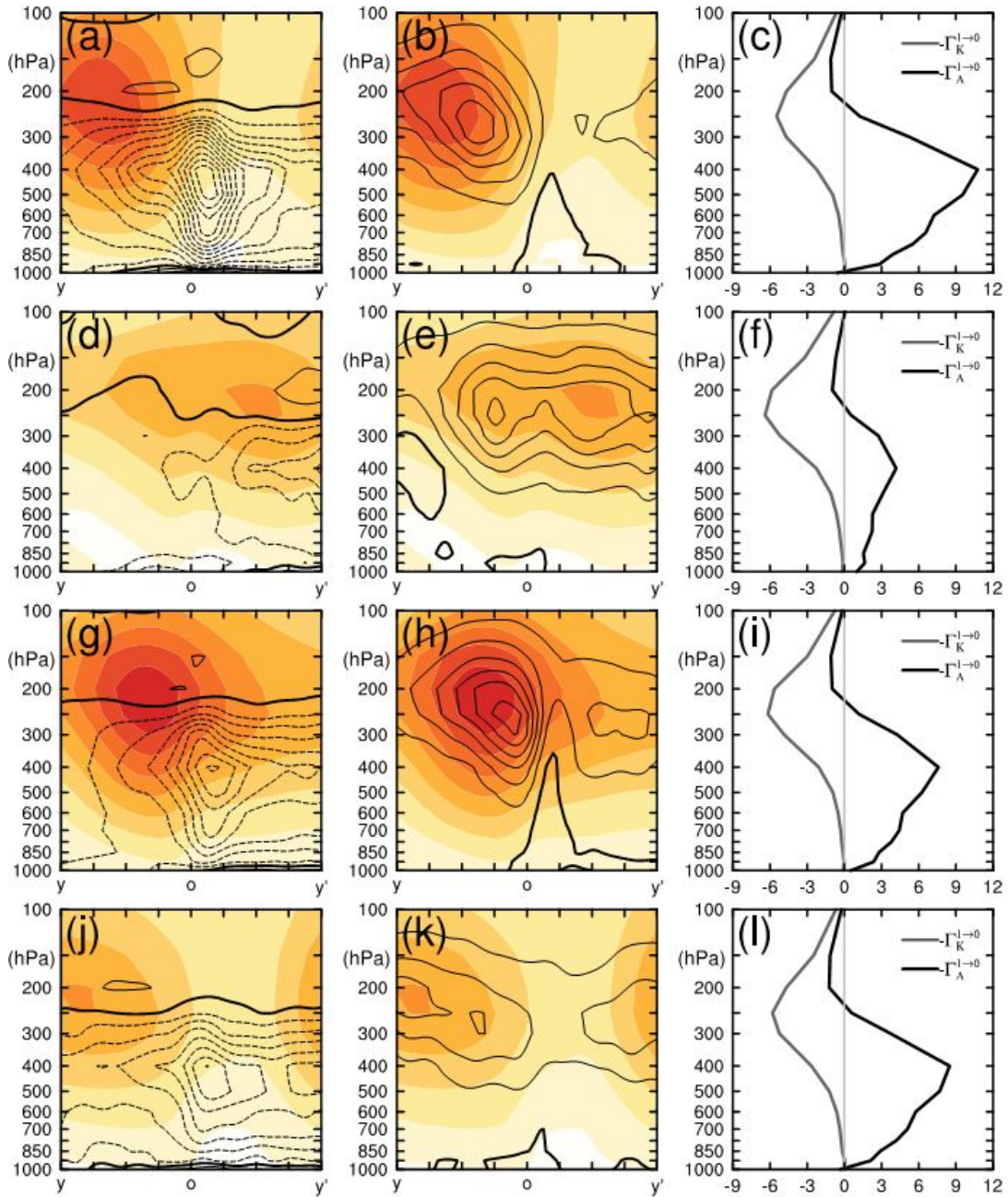
1  
2  
3  
4  
5  
6  
7  
8  
9  
10  
11  
12  
13  
14  
15  
16  
17  
18  
19  
20  
21  
22  
23  
24  
25  
26  
27  
28  
29  
30  
31  
32  
33  
34  
35  
36  
37  
38  
39  
40  
41  
42  
43  
44  
45  
46  
47  
48  
49  
50  
51  
52  
53  
54  
55  
56  
57  
58  
59  
60

550 Table 1 The average  $\Gamma_A^{0 \rightarrow 1}$  and  $\Gamma_K^{0 \rightarrow 1}$  for the four types of storms and the corresponding  
551 absolute ratio  $|\Gamma_A^{0 \rightarrow 1} / \Gamma_K^{0 \rightarrow 1}|$ .

	Type-1	Type-2	Type-3	Type-4
$\Gamma_A^{0 \rightarrow 1}$ ( $10^{-4} \text{ m}^2 \text{ s}^{-3}$ )	5.3	1.5	3.7	3.5
$\Gamma_K^{0 \rightarrow 1}$ ( $10^{-4} \text{ m}^2 \text{ s}^{-3}$ )	-1.9	-2.1	-2.1	-1.7
$ \Gamma_A^{0 \rightarrow 1} / \Gamma_K^{0 \rightarrow 1} $	2.7	0.7	1.8	2.0

552

For Peer Review



553

554 Figure 13. Same as Figures 5 and 6, but for the Type-1 storm (a, b, c), Type-2 storm (d, e,

555 f), Type-3 storm (g, h, i), and Type-4 storm (j, k, l), respectively. Left column:  $\Gamma_A^{1 \to 0}$ ;

556 Middle column:  $\Gamma_K^{1 \to 0}$ . The corresponding distributions of the standard deviations are

557 given in Figure S11 in the supplementary file.

558 Figure 13 gives the distributions of  $\Gamma_A^{1 \to 0}$  and  $\Gamma_K^{1 \to 0}$  over the meridional section

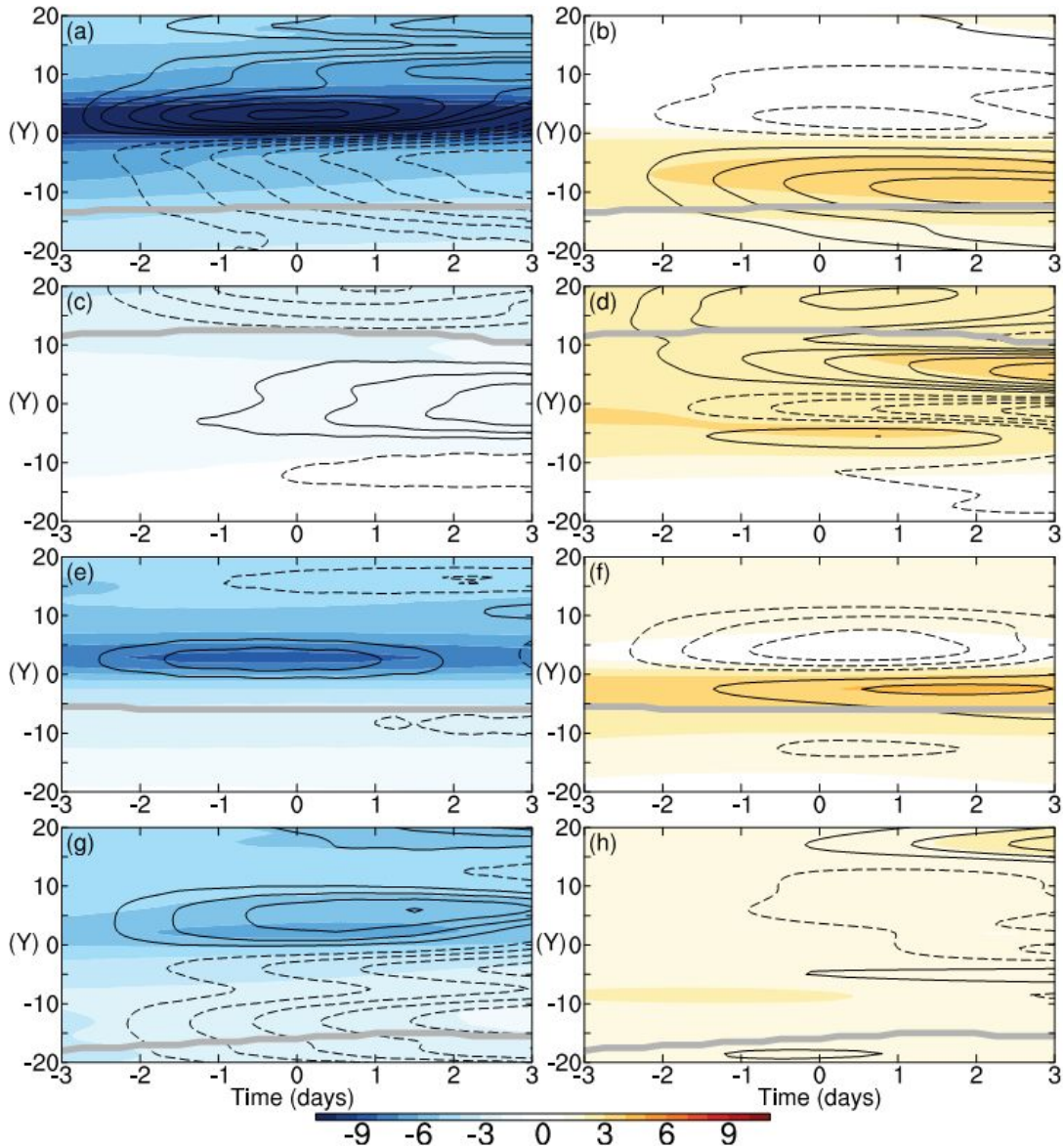
559

560

1  
2  
3  
4 559 through the storm center. For  $\Gamma_A^{1 \rightarrow 0}$ , there is always an active center on the northern side  
5  
6  
7 560 of the Type-1 (Figure 13a), Type-3 (Figure 13g), and Type-4 (Figure 13j) storms (also  
8  
9 561 the jets), whereas it is lacked in the Type-2 storm (Figure 13d). For  $\Gamma_K^{1 \rightarrow 0}$ , its center  
10  
11 562 generally coincides with the jet stream. In addition,  $\Gamma_K^{1 \rightarrow 0}$  seems to be enhanced in the  
12  
13  
14 563 southern part of the storm. For instance, the  $\Gamma_K^{1 \rightarrow 0}$  maximum always occurs there,  
15  
16  
17 564 although the jet sometime is located in the north (see Figure 13e). Vertically, the  
18  
19 565 distributions of  $\Gamma_A^{1 \rightarrow 0}$  and  $\Gamma_K^{1 \rightarrow 0}$  (Figures 13c, f, i, l) are basically the same as the  
20  
21  
22 566 mean-to-eddy counterparts (Figures 12c, f, i, l), but with the opposite sign.

23  
24  
25 567 The time evolution of the vertically averaged  $\Gamma_A^{1 \rightarrow 0}$  and  $\Gamma_K^{1 \rightarrow 0}$  is given in Figure 14.  
26  
27 568 Generally, the evolutions of Type 1, Type 3, and Type 4 are similar, with  $\Gamma_A^{1 \rightarrow 0}$  ( $\Gamma_K^{1 \rightarrow 0}$ )  
28  
29  
30 569 strengthened in the north (south) of the storm and weakened in the south (north). In  
31  
32  
33 570 contrast, Type 2 is different. Its  $\Gamma_A^{1 \rightarrow 0}$  is strengthened near the storm center and is  
34  
35  
36 571 weakened in the south and north (Figure 14c), whereas the  $\Gamma_K^{1 \rightarrow 0}$  changes in the opposite  
37  
38 572 direction (Figure 14d).





573

574 Figure 14. Same as Figs. 7a and 7b, but for the Type-1 storm (a, b), Type-2 storm (c, d),

575 Type-3 storm (e, f), and Type-4 storm (g, h). Left column:  $\Gamma_A^{1 \rightarrow 0}$ ; right column:  $\Gamma_K^{1 \rightarrow 0}$ .

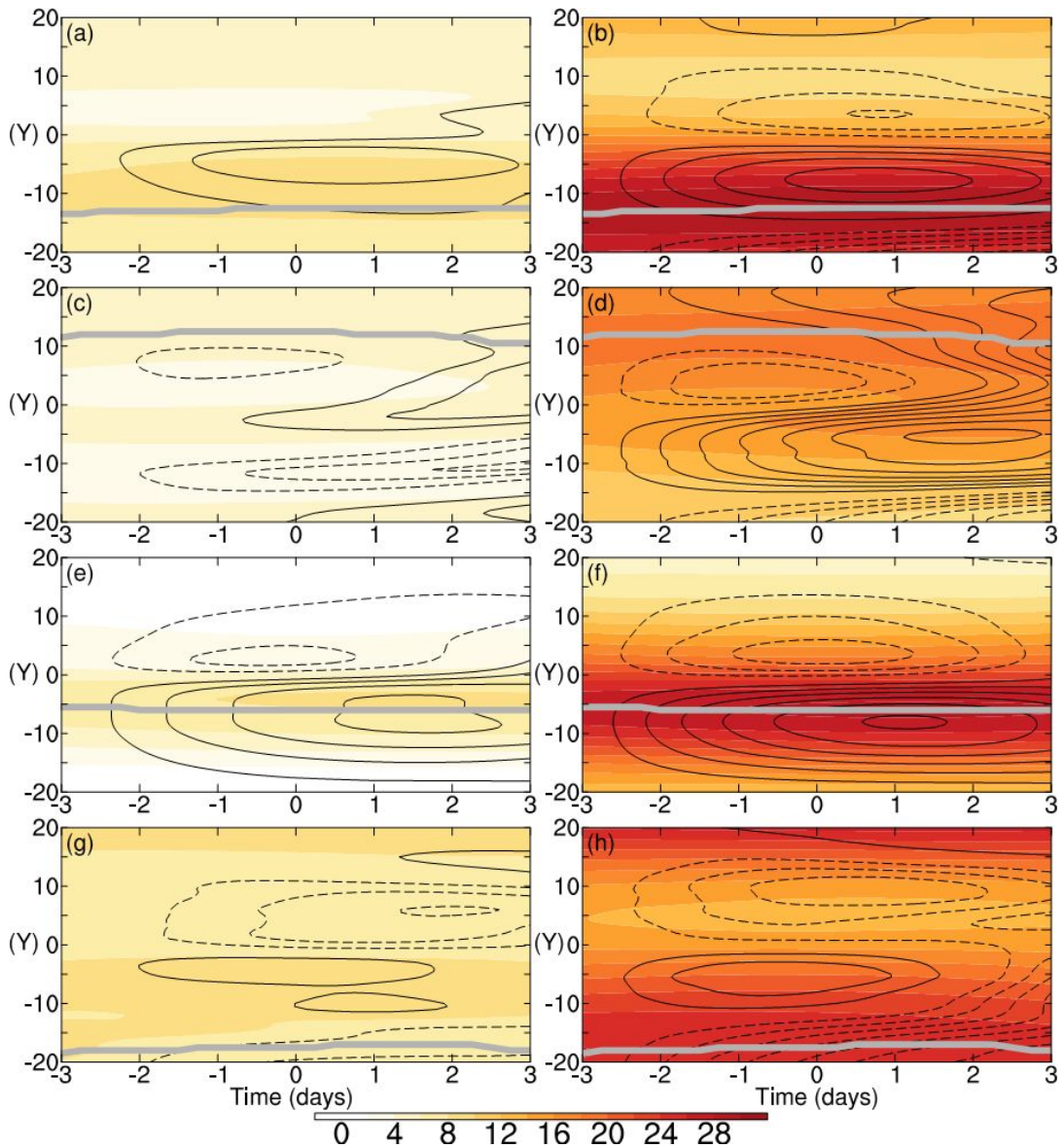
576 The thick gray curve denotes the latitude of the maximum of the 300-hPa background

577 wind. The corresponding distributions of the standard deviations are given in Figure S12

578 in the supplementary file.

579 To show the response of the background wind, displayed in Figure 15 is the time

1  
2  
3  
4 580 evolution of the background wind speed at the lower and upper tropospheric levels.  
5  
6  
7 581 Under the influence of the storm (of any type), the background wind speed is weakened  
8  
9  
10 582 in the north of the storm and is strengthened in the south, showing an anomalous dipolar  
11  
12 583 distribution. Besides, the background wind response basically shows an equivalent  
13  
14 584 barotropic structure in the vertical direction, and the response is most prominent at upper  
15  
16  
17 585 levels. It is worth noting that the Type-1, Type-3, and Type-4 storms are located near and  
18  
19  
20 586 to the north of the jet center, thus accelerating the jet, whereas the Type-2 storm is  
21  
22 587 located on the south side of the jet center, weakening the jet. In addition, the wind  
23  
24  
25 588 response to the Type-2 storm is more complex than the other three types (see Figures 15c,  
26  
27  
28 589 d). In general, the response of the background wind speed is consistent with that of the  
29  
30 590 canonical transfers, except for Type 2, implying that other processes may also play a role  
31  
32 591 for this type of storms (refer to sec. 7).  
33  
34  
35  
36  
37  
38  
39  
40  
41  
42  
43  
44  
45  
46  
47  
48  
49  
50  
51  
52  
53  
54  
55  
56  
57  
58  
59  
60



592

593 Figure 15. Same as Fig. 8a, but for the Type-1 storm (a, b), Type-2 storm (c, d), Type-3  
 594 storm (e, f), and Type-4 storm (g, h), respectively. Left column: 850 hPa; Right column:  
 595 300 hPa. The thick gray curve denotes the latitude of the maximum of the 300-hPa  
 596 background wind. The corresponding distributions of the standard deviations are given in  
 597 Figure S13 in the supplementary file.

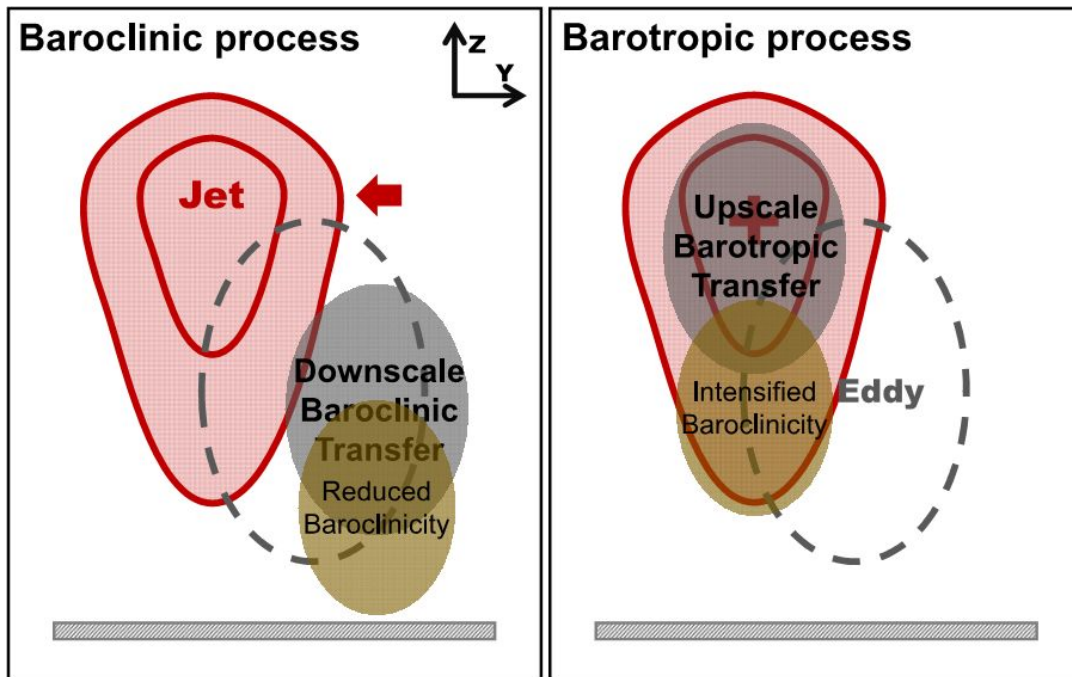
598 To summarize, all the four types of storms basically exhibit a north-south

1  
2  
3  
4 599 asymmetry in the interaction with the background flow, especially when the storm  
5  
6  
7 600 appears near or to the north of the jet center. When the storm lies to the south of the jet,  
8  
9  
10 601 the baroclinic canonical transfer turns out to be weak and its overall transfer is also  
11  
12 602 weakened, quite different from the other three types. The response of the background  
13  
14 603 wind field to the four types of storms generally exhibits a north-south oriented dipolar  
15  
16  
17 604 distribution, with positive anomaly in the south and negative anomaly in the north. But  
18  
19  
20 605 the Type-1, Type-3, and Type-4 storms strengthen the jet stream<sup>1</sup>, whereas the Type-2  
21  
22 606 storm weakens the jet stream.

23  
24  
25 607 In a word, the interaction and background wind response for the Type-1, Type-3,  
26  
27 608 and Type-4 storms are essentially similar to what we have obtained previously with all  
28  
29  
30 609 the storms considered together. The discrepancy is with the Type-2 storm. However, it  
31  
32  
33 610 should be noted that here the sample for this type is too small (with only 93 members). Its  
34  
35  
36 611 contribution is hence relatively limited and, besides, the reliability of the result also needs  
37  
38 612 to be further verified.

---

55  
56 <sup>1</sup> For the Type-4 storm, the strengthening of the background wind at upper level happens on the northern flank of the  
57 jet.  
58  
59  
60



613

614 **Figure 16.** Schematic of the typical eddy feedback in the North Pacific storm track: (left)

615 the baroclinic processes, and (right) the barotropic processes. Red and dashed gray

616 contours denote the jet and the synoptic eddy, respectively. The gray shaded area stands

617 for the canonical energy transfer centers, and the yellow shaded area are that with

618 baroclinicity change. The arrow in the left panel indicates the shrinking of the jet, and the

619 plus sign in the right panel indicates the jet acceleration.

620 **9. Conclusions**

621 Using a recently developed methodology, namely, the Multiscale Window

622 Transform (MWT) and the MWT-based localized multiscale energetics analysis and

623 vorticity analysis (MS-EVA), and an eddy tracking and compositing technique, this study

624 investigates the general structure of the nonlinear interaction between the individual

625 synoptic eddies and the jet stream over the North Pacific storm track, based on the

1  
2  
3  
4 626 ERA40 reanalysis data from ECWMF.

5  
6  
7 627 It is found that in the North Pacific storm track, more than 50% (Type 1 and Type 4)  
8  
9 628 of the storms happen on the northern flank of the jet, about 40% are near the jet center,  
10  
11 629 with very few occurring south of the jet (less than 5%). For the latter, the baroclinic  
12  
13 630 canonical transfer is rather weak. For the former two types of storms (near or to the north  
14  
15 631 of the jet center), their interaction with the background flow is quite asymmetric in space.  
16  
17 632 Specifically, the storms experience in the north a strong downscale canonical transfer of  
18  
19 633 APE, which weakens the baroclinicity and the background wind, while in the south, a  
20  
21 634 strong upscale canonical transfer of KE happens at the jet core which accelerates the jet  
22  
23 635 and enhances the baroclinicity. The resultant effect is that the jet strengthens but narrows,  
24  
25 636 resulting in an anomalous dipolar pattern in the background wind and baroclinicity field.  
26  
27 637 The general interaction scenario is schematized in Figure 16. (Note that the response of  
28  
29 638 the jet may also be partially due to other processes such as large scale energy fluxes.) On  
30  
31 639 average, the local interaction begins from about 3 days before a storm arrives at the site  
32  
33 640 of observation, achieves its maximum as the storm arrives, and then weakens.  
34  
35  
36  
37  
38  
39  
40  
41  
42

43 641 In this study, the eddy-mean flow interaction has been investigated within the whole  
44  
45 642 north Pacific storm track throughout the entire cold season (October-April) without  
46  
47 643 considering the spatiotemporal variability, which is worth further investigation. As we  
48  
49 644 know, the strength and latitudinal location of the jet change remarkably with time  
50  
51 645 throughout the year (e.g., the jet is strong and located more equatorward in winter  
52  
53 646 whereas weak and located more poleward in summer). Changes in the jet's strength and  
54  
55  
56  
57  
58  
59  
60

1  
2  
3  
4 647 latitudinal location may lead to different eddy-mean flow interactions (Chang, 2001a;  
5  
6  
7 648 Harnik and Chang, 2004; Nakamura, 1992; Penny et al., 2013; [Zhao and Liang, 2018](#)).  
8  
9 649 Besides, the eddy-mean flow interaction in the Atlantic sector may have a different  
10  
11 650 scenario, which is for sure worth investigating. Previous studies have shown that the  
12  
13  
14 651 Pacific jet is more subtropical (Lee and Kim, 2003) whereas the Atlantic jet is largely  
15  
16  
17 652 eddy driven (Woollings et al., 2010). Both the Atlantic jet and storm track are more  
18  
19  
20 653 southwest-northeast tilted than their counterparts over the Pacific. Moreover, it has been  
21  
22 654 shown (Franzke et al., 2011; Novak et al., 2015; Woollings et al., 2010) that the  
23  
24  
25 655 wintertime North Atlantic jet exhibits significant latitudinal variability, with evidence of  
26  
27  
28 656 three preferred latitudinal locations: south, middle, and north; the corresponding  
29  
30 657 storm-track characteristics may be quite different, suggesting a probably more complex  
31  
32  
33 658 eddy-mean flow interaction pattern in the Atlantic sector. We will explore these problems  
34  
35  
36 659 in our next-step studies.

660

40 661 **Appendix A. A brief introduction of multiscale window transform, canonical**  
41  
42  
43 662 **transfer, and local Lorenz cycle**

44  
45  
46 663 In this appendix, we present the needed mathematical formulas for the analysis. A  
47  
48 664 detailed introduction of the methodologies is beyond the scope here; for that purpose,  
49  
50  
51 665 refer to Liang (2016) and [Liang and Anderson \(2007\)](#). In [Xu and Liang \(2017\)](#), there is a  
52  
53  
54 666 [brief comparison to the traditional energetics in the Reynolds framework](#).

55  
56 667 *A.1 Multiscale window transform*

1  
2  
3  
4 668 As is well known, multiscale energetics formulated with time mean (resp. zonal  
5  
6  
7 669 mean) do not have information in time (resp. longitude). These formalisms, or Reynolds  
8  
9  
10 670 decomposition-based formalisms as called, cannot be used to study the energy burst  
11  
12 671 processes which are generally localized in space and time. During past decades, a  
13  
14 672 common practice is to use filtering to replace the time averaging in these formalisms. For  
15  
16 673 example, application of a low-pass filter to a velocity field  $u(t)$  yields a slowly varying  $\bar{u}$   
17  
18 674 ( $t$ ), and a high-pass filter to it gives a fast varying eddy part  $u'(t)$ :  $u(t) = \bar{u}(t) + u'(t)$ .  
19  
20  
21  
22 675 Now time dependence is retained in both fields, and hence seemingly the local  
23  
24 676 information is retained. Entailing is, however, a very basic physical question: What are  
25  
26 677 the mean energy and eddy energy with this decomposition? When  $\bar{u}$  is time invariant,  
27  
28  
29  
30 678 this is a Reynolds decomposition, we know the eddy energy is  $\overline{[u'(t)]^2}$ ; now if  $\bar{u}$  is time  
31  
32 679 varying, what is the eddy energy then? During the past 2-3 decades, a common practice  
33  
34 680 in the literature is simply to take it as  $[u'(t)]^2$ . That corresponds to, in the Reynolds  
35  
36 681 decomposition case, a relieving of the time mean in the eddy energy  $\overline{[u'(t)]^2}$ .

40 682 This is, unfortunately, conceptually incorrect. To illustrate, consider a very simple  
41  
42  
43 683 example which has a Fourier expansion

$$u(t) = \bar{u}(t) + u'(t) = [a_0 \cos \omega_0 t] + [a_1 \cos \omega_1 t], \quad \omega_1 > \omega_0,$$

48 684 with subscripts 0, 1 representing the slow and fast processes, respectively. Now what are  
49  
50  
51 685 the energies for these processes? In this simple case we know they should be,  
52  
53 686 respectively,  $a_0^2$  and  $a_1^2$ . That is to say, multiscale energy is a concept in phase space;  
54  
55  
56 687 here they are functions of the Fourier coefficients  $(a_0, a_1)$ . By the common practice with



1  
2  
3  
4 688 filters as shown above, however, the energies would be simply taken as

$$5 \quad 6 \quad 7 \quad 8 \quad [\bar{u}(t)]^2 = [a_0 \cos \omega_0 t]^2 \quad \text{and} \quad [u'(t)]^2 = [a_1 \cos \omega_1 t]^2$$

9 689 which are functions of the reconstructions or filtered parts in physical space!

10  
11 690 So the common practice during the past decades is conceptually incorrect.

12  
13 691 Multiscale energy is a concept in phase space; it is related to its physical space

14  
15 692 counterpart through the famous Parseval equality. Mathematically it is the square of the

16  
17 693 norm of a field variable, or, alternatively, the Fourier transform of an autocorrelation

18  
19 694 function (e.g., Batchelor, 1953). In the above example, when  $\omega_0 = 0$ , it is easy to prove

20  
21 695 that  $a_1^2 = \overline{[u'(t)]^2}$ , just as that with the Reynolds decomposition. From this example *one*

22  
23 696 *also sees that the time mean in the classical Reynolds formalism is essential; it cannot be*

24  
25 697 *removed to pretend to gain the time variability.* In fact, it is by no means a trivial task to

26  
27 698 have the local energy of a time-dependent filtered field faithfully represented; it is a

28  
29 699 rather profound problem. This even has not been possible until filter banks and wavelets

30  
31 700 are connected (Strang and Nguyen, 1996), and has just been systematically addressed by

32  
33 701 Liang and Anderson (2007) in the development of multiscale window transform (MWT).

34  
35 702 MWT is a tool that helps decompose a function space into a direct sum of

36  
37 703 orthogonal subspaces, each with an exclusive range of scales (represented by wavelet

38  
39 704 scale levels), while having the local information retained. Such a subspace is termed a

40  
41 705 *scale window*, or simply a window. MWT can be viewed as a generalization of the

42  
43 706 classical Reynolds decomposition; originally it is developed for representing the energies

44  
45 707 (and any quadratic quantities) on the resulting scale windows, in order to make multiscale

1  
2  
3  
4 708 energetics analysis possible. Liang and Anderson (2007) find that, for some specially  
5  
6 709 constructed orthogonal<sup>1</sup> filters, there exists a transfer-reconstruction pair, namely, MWT  
7  
8  
9 710 and its counterpart multiscale window reconstruction (MWR). In some sense MWR  
10  
11 711 functions just like a filter in the traditional sense. What makes it different is that, for each  
12  
13  
14 712 MWR, there exists an MWT which gives coefficients that can be used to represent the  
15  
16  
17 713 energy of the filtered series. In this way multiscale energetics analysis is made possible.

18  
19  
20 714 In MWT, a scale window is demarcated by two scale levels, or window bounds. For  
21  
22 715 a time series with a duration  $\tau$ , a scale level  $j$  corresponds to a period  $2^{-j}\tau$ . In the  
23  
24  
25 716  $M$ -window case, the windows are bounded above by  $M+1$  scale levels:  $j_0, j_1, \dots, j_M$ .  
26  
27 717 Alternatively,  $2^{-j_0}\tau, 2^{-j_1}\tau, \dots, 2^{-j_M}\tau$  are the time scale bounds. For convenience, we  
28  
29  
30 718 will denote them by  $\varpi = 0, 1, \dots, M$  respectively.

31  
32 719 Now suppose  $\{\varphi_n^j(t)\}_n$  is an orthonormal translational invariant scaling sequence  
33  
34  
35 720 (built from cubic splines; see Liang and Anderson (2007), and Figure 1 in Liang (2016)),  
36  
37  
38 721 with  $j$  some wavelet scale level and  $n$  the time step. Let  $T(t)$  be some square integrable  
39  
40  
41 722 function defined on  $[0,1]$  (if not, the domain can always be rescaled to  $[0,1]$ ). It has been  
42  
43  
44 723 shown (Liang and Anderson 2007) that all such functions can be practically represented  
45  
46  
47 724 using  $\{\varphi_n^j(t)\}_n$  as a basis. In doing this, there is a scaling transform

$$\hat{T}_n^j = \int_0^1 T(t)\varphi_n^j(t)dt$$

---

54  
55 <sup>1</sup> Note here *orthogonality* is crucial; otherwise Parseval's relation does not hold and hence energy  
56 cannot even be defined.

for any scale level  $j$  (corresponding to frequency  $2^j$ ). Given window bounds  $j_0, j_1$  for a two-window decomposition,  $T$  then can be reconstructed on the windows formed above:

$$T^{\sim 0}(t) = \sum_{n=0}^{2^{j_0}-1} \hat{T}_n^{j_0} \varphi_n^{j_0}(t),$$

$$T^{\sim 1}(t) = \sum_{n=0}^{2^{j_1}-1} \hat{T}_n^{j_1} \varphi_n^{j_1}(t) - T^{\sim 0}(t),$$

with the notations  $\sim 0, \sim 1$  signifying the corresponding scale windows. With these reconstructions (multiscale window reconstruction, or MWR for short), the MWT of  $T$  is defined as

$$\hat{T}_n^{\sim \varpi} = \int_0^1 T^{\sim \varpi}(t) \varphi_n^{j_1}(t) dt,$$

for windows  $\varpi = 0, 1$  and  $n = 0, 1, \dots, N$ , and  $N = 2^{j_1} - 1$ . In terms of  $\hat{T}_n^{\sim \varpi}$  the above reconstructions on the two windows can be written in a unified way:

$$T^{\sim \varpi}(t) = \sum_{n=0}^{2^{j_1}-1} \hat{T}_n^{\sim \varpi} \varphi_n^{j_1}(t).$$

These two equations make a transform-reconstruction pair for the MWT. Note that the  $T^{\sim \varpi}(t)$  are just like the low/high-pass filtered quantities which are defined in physical space, while the transform coefficients  $\hat{T}_n^{\sim \varpi}$  (just like Fourier coefficients) can be used to represent multiscale energy---it has been rigorously proved that the energy on scale  $\varpi$  is precisely equal to the square of the MWT coefficients (up to some constant multiplier). Note it is by no means as trivial as  $[T^{\sim \varpi}(t)]^2$ , which has been frequently seen in the literature.

*A.2 Multiscale energetics and local Lorenz cycle*

1  
2  
3  
4 740 Following Liang (2016), consider the primitive equations in an isobaric coordinate  
5  
6  
7 741 frame:

$$\frac{\partial \mathbf{v}_h}{\partial t} + \mathbf{v}_h \cdot \nabla_h \mathbf{v}_h + \omega \frac{\partial \mathbf{v}_h}{\partial p} + f \mathbf{k} \times \mathbf{v}_h = -\nabla_h \Phi + \mathbf{F} \quad (\text{A1})$$

$$\frac{\partial \Phi}{\partial p} = -\alpha \quad (\text{A2})$$

$$\nabla_h \cdot \mathbf{v}_h + \frac{\partial \omega}{\partial p} = 0 \quad (\text{A3})$$

$$\frac{\partial T}{\partial t} + \mathbf{v}_h \cdot \nabla_h T + \omega \frac{\partial T}{\partial p} + \omega \bar{\alpha} \frac{L - L_d}{g} + \omega \alpha \frac{L - L_d}{g} = \frac{\dot{q}_{net}}{c_p} \quad (\text{A4})$$

$$p\alpha = RT \quad (\text{A5})$$

22 742 where  $L$  is the lapse rate and  $L_d$  the lapse rate for dry air, the subscript h stands for  
23  
24 743 horizontal direction and the overbar for mean over time and over the isobaric plane. The  
25  
26  
27 744 other notations are conventional. Note here  $\Phi$  (geopotential) and  $\alpha$  (specific volume) are  
28  
29  
30 745 anomalies; their time averages have been pre-subtracted.

31  
32 746 With MWT, the available potential energy (APE) and kinetic energy (KE) densities  
33  
34  
35 747 (for convenience, we will simply refer to them as APE and KE, unless confusion may  
36  
37  
38 748 arise) on window  $\varpi$  at location  $n$  can be defined, following Lorenz (1955), as

$$A^\varpi = \frac{1}{2} c (\hat{T}^{\sim\varpi})^2, \quad (\text{A6})$$

$$K^\varpi = \frac{1}{2} \hat{\mathbf{v}}_h^{\sim\varpi} \cdot \hat{\mathbf{v}}_h^{\sim\varpi}. \quad (\text{A7})$$

45  
46 749 Note here the subscript  $n$  has been suppressed for clarity; same below. From Eqs.  
47  
48 750 (A1)-(A5) the evolutionary equations for  $K^\varpi$  and  $A^\varpi$  for windows  $\varpi$  ( $=0, 1, \dots$ ) can  
49  
50  
51 751 be obtained; they are Eqs. (1) and (2), which we rewrite as follows:

$$\frac{\partial K^\varpi}{\partial t} + \nabla \cdot \mathbf{Q}_K^\varpi = \Gamma_K^\varpi - \nabla \cdot \mathbf{Q}_P^\varpi + b^\varpi + F_K^\varpi \quad (\text{A8})$$

$$\frac{\partial A^\varpi}{\partial t} + \nabla \cdot \mathbf{Q}_A^\varpi = \Gamma_A^\varpi - b^\varpi + S_A^\varpi + F_A^\varpi \quad (\text{A9})$$

752 The physical explanations and mathematical expressions for these terms are listed in

753 Table A1.

754

755 **Table A1.** The energetic terms in Equations (A8)-(A9). The colon operator ( $:$ ) in  $\Gamma_K^\varpi$  and

756  $\Gamma_A^\varpi$  is defined such that, for two dyadic products  $\mathbf{AB}$  and  $\mathbf{CD}$ ,  $(\mathbf{AB}):(\mathbf{CD}) = (\mathbf{A} \cdot \mathbf{C})(\mathbf{B} \cdot$

757  $\mathbf{D})$ . If total energetics (in  $\mathbf{W}$ ) are to be computed, the resulting integrals with respect to  $(x,$

758  $y, p)$  should be divided by  $g$ . Besides, all terms are to be multiplied by  $2^{j_1}$ , which is

759 omitted for notational simplicity.

Symbol	Mathematical expression	Physical interpretation
$K^\varpi$	$\frac{1}{2} \hat{\mathbf{v}}_h^{\sim\varpi} \cdot \hat{\mathbf{v}}_h^{\sim\varpi}$	KE on scale window $\varpi$
$\mathbf{Q}_K^\varpi$	$\frac{1}{2} (\widehat{\mathbf{v}\mathbf{v}}_h)^{\sim\varpi} \cdot \hat{\mathbf{v}}_h^{\sim\varpi}$	Flux of KE on window $\varpi$
$\Gamma_K^\varpi$	$\frac{1}{2} [(\widehat{\mathbf{v}\mathbf{v}}_h)^{\sim\varpi} : \nabla \hat{\mathbf{v}}_h^{\sim\varpi} - \nabla \cdot (\widehat{\mathbf{v}\mathbf{v}}_h)^{\sim\varpi} \cdot \hat{\mathbf{v}}_h^{\sim\varpi}]$	Canonical transfer of KE to window $\varpi$
$\mathbf{Q}_p^\varpi$	$\hat{\mathbf{v}}^{\sim\varpi} \hat{\phi}^{\sim\varpi}$	Geopotential flux
$b^\varpi$	$-\hat{\omega}^{\sim\varpi} \hat{\alpha}^{\sim\varpi}$	Buoyancy conversion
$A^\varpi$	$\frac{1}{2} c (\hat{\mathbf{T}}^{\sim\varpi})^2, c = \frac{g}{\bar{T}(g/C_p - L)}$	APE on scale window $\varpi$
$\mathbf{Q}_A^\varpi$	$\frac{1}{2} c \hat{\mathbf{T}}^{\sim\varpi} (\widehat{\mathbf{v}\mathbf{T}})^{\sim\varpi}$	Flux of APE on window $\varpi$
$\Gamma_A^\varpi$	$\frac{c}{2} [(\widehat{\mathbf{v}\mathbf{T}})^{\sim\varpi} \cdot \nabla \hat{\mathbf{T}}^{\sim\varpi} - \hat{\mathbf{T}}^{\sim\varpi} \nabla \cdot (\widehat{\mathbf{v}\mathbf{T}})^{\sim\varpi}]$	Canonical transfer of APE to window $\varpi$
$S_A^\varpi$	$\frac{1}{2} \hat{\mathbf{T}}^{\sim\varpi} (\widehat{\omega\mathbf{T}})^{\sim\varpi} \frac{\partial c}{\partial p} + \frac{1}{\bar{T}} \hat{\omega} \hat{\alpha}^{\sim\varpi}$	Apparent source/sink (usually negligible)

760

1  
2  
3  
4 761 Among those terms in Table A1 are  $\Gamma_A^\varpi$  and  $\Gamma_K^\varpi$ , which represent the transfers of  
5  
6 762 APE and KE between the scale windows and hence make the processes that we are most  
7  
8  
9 763 interested in for this study. For a scalar field  $T$  (may be any scalar field or component of  
10  
11  
12 764 vector field; not necessarily temperature) in a flow  $\mathbf{v}$ , the energy transfer from other  
13  
14  
15 765 scale windows to window  $\varpi$  is (see Liang (2016) for a rigorous proof)

$$\Gamma_n^\varpi = -E_n^\varpi \nabla \cdot \mathbf{v}_T^\varpi = \frac{1}{2} [(\widehat{\mathbf{v}T})_n^{\sim\varpi} \cdot \nabla \hat{T}_n^{\sim\varpi} - \hat{T}_n^{\sim\varpi} \nabla \cdot (\widehat{\mathbf{v}T})_n^{\sim\varpi}], \quad (\text{A10})$$

16  
17  
18  
19  
20 766 where  $E^\varpi = \frac{1}{2}(\hat{T}^{\sim\varpi})^2$  is the energy of window  $\varpi$ .<sup>1</sup> The other symbol

$$\mathbf{v}_T^\varpi = \frac{(\widehat{\mathbf{v}T})_n^{\sim\varpi}}{\hat{T}_n^{\sim\varpi}} \quad (\text{A11})$$

21  
22  
23  
24  
25  
26 767 is referred to as the *T-coupled velocity*, which can be understood as the weighted average  
27  
28  
29 768 of  $\mathbf{v}$  in the phase space of MWT. With this, the transfer of APE and KE can be easily  
30  
31  
32 769 obtained. For example,

$$\Gamma_K^\varpi = -\frac{1}{2} [(\hat{u}^{\sim\varpi})^2 \nabla \cdot \mathbf{v}_u^\varpi + (\hat{v}^{\sim\varpi})^2 \nabla \cdot \mathbf{v}_v^\varpi] \quad (\text{A12})$$

33  
34  
35  
36  
37 770 which can be proved to be that in Table A1.

38  
39 771 The so-obtained transfer possesses a very interesting property, namely

$$\sum_{\varpi} \sum_n \Gamma_n^\varpi = 0, \quad (\text{A13})$$

40  
41  
42  
43  
44  
45 772 as first proposed in Liang and Robinson (2005) and later proved in Liang (2016).

46  
47  
48 773 Physically, this implies that the transfer is a mere redistribution of energy among the  
49  
50  
51 774 scale windows, without generating or destroying energy as a whole. This property,

---

52  
53  
54  
55 <sup>1</sup> When needed, a constant should be multiplied on both sides. For example, if  $T$  is temperature, then  
56  $E^\varpi$  and  $\Gamma^\varpi$  should be both multiplied by  $c$  to make APE and APE transfer.

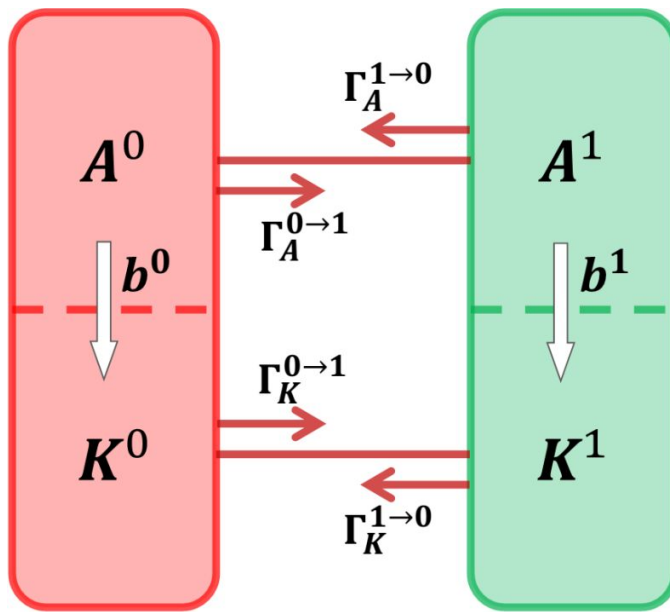
1  
2  
3  
4 775 though simple to state, does not hold in previous time decomposition-based or  
5  
6  
7 776 Lorenz-type energetics formalisms (refer to Liang and Robinson (2007) for a clear  
8  
9  
10 777 comparison to the classical formalism). To distinguish it from those that may have been  
11  
12 778 encountered in the literature, it is termed *canonical transfer*.

13  
14 779 As shown in Liang (2016), a canonical transfer has a *Lie bracket form*; it satisfies  
15  
16  
17 780 the *Jacobian identity*, reminiscent of the *Poisson bracket in Hamiltonian mechanics*. It  
18  
19  
20 781 also satisfies a “*detailed balance relation*”, which usually results from the Saltzman-type  
21  
22  
23 782 or space decomposition-based energetics formalisms (Liang and Robinson 2005).

24  
25 783 So, for an ideal fluid, the energetic processes represented in (A8)-(A9) are all  
26  
27  
28 784 conservative. In other words, a local Lorenz cycle in the absence of dissipation and  
29  
30 785 diffusion is composed of [the following three types of processes](#):

- 31  
32  
33 786 ● transports: redistributing energy in space (vanishing if integrated over a closed  
34  
35 787 domain),  
36  
37  
38 788 ● canonical transfers: redistributing energy among scale windows (vanishing if  
39  
40 789 summarized over scale windows and locations),  
41  
42  
43 790 ● buoyancy conversion: redistributing energy between APE and KE.

44  
45  
46 791 Figure A1 schematizes these processes for a two-window decomposition. Note here the  
47  
48 792 [arrows connecting  \$K^0\(A^0\)\$  and  \$K^1\(A^1\)\$  are the quantities](#) that are difficult to diagnose  
49  
50  
51 793 with the traditional methods.



794

795 **Figure A1.** The local Lorenz cycle for a two-window decomposition (the scale windows  
 796 are denoted in the superscripts as 0 and 1, respectively). For clarity, transports and  
 797 dissipative/diffusive processes are not shown.

798 Note a canonical transfer may involve contributions from essentially all scale  
 799 windows; it is necessary to differentiate them. Consider for an example window  $\varpi = 1$ .  
 800 The energy transferred to the window can be from window 0 and itself  $\varpi = 1$ . Since all  
 801 canonical transfers are linear combinations of terms in a triple product form:

$$\Gamma_n^1 = \hat{\mathcal{R}}_n^1 (\widehat{pq})_n^{\sim 1}$$

802 it suffices to consider  $\Gamma_n^1$ . From Liang (2016), it is

$$\Gamma_n^1 = \hat{\mathcal{R}}_n^1 \left[ (\widehat{p^0 q^0})_n^{\sim 1} + (\widehat{p^0 q^1})_n^{\sim 1} + (\widehat{p^1 q^0})_n^{\sim 1} \right] + \hat{\mathcal{R}}_n^1 (\widehat{p^1 q^1})_n^{\sim 1}$$

803 where the first part on the right hand side is the canonical energy transfer from window 0  
 804 to window 1; write it as  $\Gamma^{0 \rightarrow 1}$ . The second part, denoted by  $\Gamma^{1 \rightarrow 1}$ , is the canonical energy  
 805 transfer to itself, which is usually very small.  $\Gamma^{0 \rightarrow 1}$  is of particular importance in that it



1  
2  
3  
4 806 is usually related to the instability in geophysical fluid dynamics; in particular,  $\Gamma_A^{0 \rightarrow 1}$  and  
5  
6 807  $\Gamma_K^{0 \rightarrow 1}$  are usually related to baroclinic instability and barotropic instability of the mean  
7  
8  
9 808 flow. For this reason, in the text sometimes  $\Gamma_A^{0 \rightarrow 1}$  and  $\Gamma_K^{0 \rightarrow 1}$  have been referred to as  
10  
11  
12 809 baroclinic canonical transfer and barotropic canonical transfer, respectively.  
13  
14  
15 810

### 17 811 **Acknowledgements**

18  
19 812 The suggestions of two anonymous reviewers are sincerely appreciated. This study was  
20  
21  
22 813 partially supported by the Jiangsu Provincial Government through the 2015 Jiangsu  
23  
24  
25 814 Program for Innovation Research and Entrepreneurship Groups and the Jiangsu Chair  
26  
27 815 Professorship to XSL, the National Natural Science Foundation of China under Grants  
28  
29  
30 816 No. 41276032 and 41705024, and the National Program on Global Change and Air-Sea  
31  
32 817 Interaction [GASI-IPOVAI-06].  
33  
34  
35 818

### 37 819 **References**

- 38  
39 820 Anderson, D., Hodges, K.I., Hoskins, B.J., 2003. Sensitivity of Feature-Based Analysis  
40 821 Methods of Storm Tracks to the Form of Background Field Removal. *Mon.*  
41 822 *Weather Rev.* 131, 565–573.  
42 823 [https://doi.org/10.1175/1520-0493\(2003\)131<0565:SOFBAM>2.0.CO;2](https://doi.org/10.1175/1520-0493(2003)131<0565:SOFBAM>2.0.CO;2)  
43 824 Andrews, D.G., McIntyre, M.E., 1978. Generalized Eliassen-Palm and Charney-Drazin  
44 825 Theorems for Waves on Axisymmetric Mean Flows in Compressible Atmospheres.  
45 826 *J. Atmospheric Sci.* 35, 175–185.  
46 827 [https://doi.org/10.1175/1520-0469\(1978\)035<0175:GEPACD>2.0.CO;2](https://doi.org/10.1175/1520-0469(1978)035<0175:GEPACD>2.0.CO;2)  
47 828 Barnes, E.A., Hartmann, D.L., 2011. Rossby Wave Scales, Propagation, and the  
48 829 Variability of Eddy-Driven Jets. *J. Atmospheric Sci.* 68, 2893–2908.  
49 830 <https://doi.org/10.1175/JAS-D-11-039.1>  
50 831 Barnes, J.R., Young, R.E., 1992. Nonlinear Baroclinic Instability on the Sphere: Multiple  
51 832 Life Cycles with Surface Drag and Thermal Damping. *J. Atmospheric Sci.* 49,

- 833 861–878. [https://doi.org/10.1175/1520-0469\(1992\)049<0861:NBIOTS>2.0.CO;2](https://doi.org/10.1175/1520-0469(1992)049<0861:NBIOTS>2.0.CO;2)
- 834 Bengtsson, L., Hodges, K.I., Esch, M., Keenlyside, N., Kornblueh, L., Luo, J.-J.,  
835 Yamagata, T., 2007. How may tropical cyclones change in a warmer climate?  
836 *Tellus A* 59, 539–561. <https://doi.org/10.1111/j.1600-0870.2007.00251.x>
- 837 Bengtsson, L., Hodges, K.I., Keenlyside, N., 2009. Will Extratropical Storms Intensify in  
838 a Warmer Climate? *J. Clim.* 22, 2276–2301.  
839 <https://doi.org/10.1175/2008JCLI2678.1>
- 840 Blackmon, M.L., 1976. A Climatological Spectral Study of the 500 mb Geopotential  
841 Height of the Northern Hemisphere. *J. Atmospheric Sci.* 33, 1607–1623.  
842 [https://doi.org/10.1175/1520-0469\(1976\)033<1607:ACSSOT>2.0.CO;2](https://doi.org/10.1175/1520-0469(1976)033<1607:ACSSOT>2.0.CO;2)
- 843 Blackmon, M.L., Lee, Y.-H., Wallace, J.M., 1984. Horizontal Structure of 500 mb Height  
844 Fluctuations with Long, Intermediate and Short Time Scales. *J. Atmospheric Sci.*  
845 41, 961–980.  
846 [https://doi.org/10.1175/1520-0469\(1984\)041<0961:HSOMHF>2.0.CO;2](https://doi.org/10.1175/1520-0469(1984)041<0961:HSOMHF>2.0.CO;2)
- 847 Blackmon, M.L., Wallace, J.M., Lau, N.-C., Mullen, S.L., 1977. An Observational Study  
848 of the Northern Hemisphere Wintertime Circulation. *J. Atmospheric Sci.* 34,  
849 1040–1053.  
850 [https://doi.org/10.1175/1520-0469\(1977\)034<1040:AOSOTN>2.0.CO;2](https://doi.org/10.1175/1520-0469(1977)034<1040:AOSOTN>2.0.CO;2)
- 851 Cai, M., M. Mak, 1990. On the Basic Dynamics of Regional Cyclogenesis. *J.*  
852 *Atmospheric Sci.*, 47, 1417–1442,  
853 [doi:10.1175/1520-0469\(1990\)047<1417:OTBDOR>2.0.CO;2](https://doi.org/10.1175/1520-0469(1990)047<1417:OTBDOR>2.0.CO;2).
- 854 Catto, J.L., Shaffrey, L.C., Hodges, K.I., 2010. Can Climate Models Capture the  
855 Structure of Extratropical Cyclones? *J. Clim.* 23, 1621–1635.  
856 <https://doi.org/10.1175/2009JCLI3318.1>
- 857 Chang, E.K.M., 2001a. GCM and Observational Diagnoses of the Seasonal and  
858 Interannual Variations of the Pacific Storm Track during the Cool Season. *J.*  
859 *Atmospheric Sci.* 58, 1784–1800.  
860 [https://doi.org/10.1175/1520-0469\(2001\)058<1784:GAODOT>2.0.CO;2](https://doi.org/10.1175/1520-0469(2001)058<1784:GAODOT>2.0.CO;2)
- 861 Chang, E. K. M., 2001b. The Structure of Baroclinic Wave Packets. *J. Atmospheric Sci.*,  
862 58, 1694–1713, [doi:10.1175/1520-0469\(2001\)058<1694:T SOBWP>2.0.CO;2](https://doi.org/10.1175/1520-0469(2001)058<1694:T SOBWP>2.0.CO;2).
- 863 Chang, E.K.M., 1993. Downstream Development of Baroclinic Waves As Inferred from  
864 Regression Analysis. *J. Atmospheric Sci.* 50, 2038–2053.  
865 [https://doi.org/10.1175/1520-0469\(1993\)050<2038:DDOBWA>2.0.CO;2](https://doi.org/10.1175/1520-0469(1993)050<2038:DDOBWA>2.0.CO;2)
- 866 Chang, E.K.M., Lee, S., Swanson, K.L., 2002. Storm Track Dynamics. *J. Clim.* 15,  
867 2163–2183. [https://doi.org/10.1175/1520-0442\(2002\)015<02163:STD>2.0.CO;2](https://doi.org/10.1175/1520-0442(2002)015<02163:STD>2.0.CO;2)
- 868 Chang, E.K.M., Orlanski, I., 1993. On the Dynamics of a Storm Track. *J. Atmospheric*  
869 *Sci.* 50, 999–1015.  
870 [https://doi.org/10.1175/1520-0469\(1993\)050<0999:OTDOAS>2.0.CO;2](https://doi.org/10.1175/1520-0469(1993)050<0999:OTDOAS>2.0.CO;2)
- 871 Charney, J.G., Drazin, P.G., 1961. Propagation of planetary-scale disturbances from the  
872 lower into the upper atmosphere. *J. Geophys. Res.* 66, 83–109.  
873 <https://doi.org/10.1029/JZ066i001p00083>

- 1  
2  
3 874 Chen, G., Plumb, R.A., 2009. Quantifying the Eddy Feedback and the Persistence of the  
4 875 Zonal Index in an Idealized Atmospheric Model. *J. Atmospheric Sci.* 66, 3707–  
5 876 3720. <https://doi.org/10.1175/2009JAS3165.1>  
6  
7 877 Dacre, H.F., Hawcroft, M.K., Stringer, M.A., Hodges, K.I., 2012. An Extratropical  
8 878 Cyclone Atlas: A Tool for Illustrating Cyclone Structure and Evolution  
9 879 Characteristics. *Bull. Am. Meteorol. Soc.* 93, 1497–1502.  
10 880 <https://doi.org/10.1175/BAMS-D-11-00164.1>  
11  
12 881 Deng, Y., Mak, M., 2006. Nature of the Differences in the Intraseasonal Variability of the  
13 882 Pacific and Atlantic Storm Tracks: A Diagnostic Study. *J. Atmospheric Sci.* 63,  
14 883 2602–2615. <https://doi.org/10.1175/JAS3749.1>  
15  
16 884 Dickinson, R.E., 1969. Theory of Planetary Wave-Zonal Flow Interaction. *J.*  
17 885 *Atmospheric Sci.* 26, 73–81.  
18 886 [https://doi.org/10.1175/1520-0469\(1969\)026<0073:TOPWZF>2.0.CO;2](https://doi.org/10.1175/1520-0469(1969)026<0073:TOPWZF>2.0.CO;2)  
19  
20 887 Edmon, H.J., Hoskins, B.J., McIntyre, M.E., 1980. Eliassen-Palm Cross Sections for the  
21 888 Troposphere. *J. Atmospheric Sci.* 37, 2600–2616.  
22 889 [https://doi.org/10.1175/1520-0469\(1980\)037<2600:EPCSFT>2.0.CO;2](https://doi.org/10.1175/1520-0469(1980)037<2600:EPCSFT>2.0.CO;2)  
23  
24 890 Eliassen, A., Palm, E., 1961. On the transfer of energy in stationary mountain waves.  
25 891 *Geophys Publ* 22, 1–23.  
26  
27 892 Farrell, B., 1984. Modal and Non-Modal Baroclinic Waves. *J. Atmospheric Sci.*, 41,  
28 893 668–673, doi:10.1175/1520-0469(1984)041<0668:MANMBW>2.0.CO;2.  
29  
30 894 —, 1985. Transient Growth of Damped Baroclinic Waves. *J. Atmospheric Sci.*, 42,  
31 895 2718–2727, doi:10.1175/1520-0469(1985)042<2718:TGODBW>2.0.CO;2.  
32  
33 896 —, 1989. Optimal Excitation of Baroclinic Waves. *J. Atmospheric Sci.*, 46, 1193–  
34 897 1206, doi:10.1175/1520-0469(1989)046<1193:OEOWB>2.0.CO;2.  
35  
36 898 Field, P.R., Wood, R., 2007. Precipitation and Cloud Structure in Midlatitude Cyclones.  
37 899 *J. Clim.* 20, 233–254. <https://doi.org/10.1175/JCLI3998.1>  
38  
39 900 Franzke, C., Woollings, T., Martius, O., 2011. Persistent Circulation Regimes and  
40 901 Preferred Regime Transitions in the North Atlantic. *J. Atmospheric Sci.* 68, 2809–  
41 902 2825. <https://doi.org/10.1175/JAS-D-11-046.1>  
42  
43 903 Gerber, E.P., Vallis, G.K., 2007. Eddy–Zonal Flow Interactions and the Persistence of the  
44 904 Zonal Index. *J. Atmospheric Sci.* 64, 3296–3311.  
45 905 <https://doi.org/10.1175/JAS4006.1>  
46  
47 906 Green, J.S.A., 1960. A problem in baroclinic stability. *Q. J. R. Meteorol. Soc.* 86, 237–  
48 907 251. <https://doi.org/10.1002/qj.49708636813>  
49  
50 908 Harnik, N., Chang, E.K.M., 2004. The Effects of Variations in Jet Width on the Growth  
51 909 of Baroclinic Waves: Implications for Midwinter Pacific Storm Track Variability.  
52 910 *J. Atmospheric Sci.* 61, 23–40.  
53 911 [https://doi.org/10.1175/1520-0469\(2004\)061<0023:TEOVII>2.0.CO;2](https://doi.org/10.1175/1520-0469(2004)061<0023:TEOVII>2.0.CO;2)  
54  
55 912 Hartmann, D.L., 1974. Time Spectral Analysis of Mid-Latitude Disturbances. *Mon.*  
56 913 *Weather Rev.* 102, 348–362.  
57 914 [https://doi.org/10.1175/1520-0493\(1974\)102<0348:TSAOML>2.0.CO;2](https://doi.org/10.1175/1520-0493(1974)102<0348:TSAOML>2.0.CO;2)  
58  
59  
60

- 1  
2  
3 915 Hodges, K.I., 1995. Feature Tracking on the Unit Sphere. *Mon. Weather Rev.* 123, 3458–  
4 916 3465. [https://doi.org/10.1175/1520-0493\(1995\)123<3458:FTOTUS>2.0.CO;2](https://doi.org/10.1175/1520-0493(1995)123<3458:FTOTUS>2.0.CO;2)  
5  
6 917 Hoskins, B.J., McIntyre, M.E., Robertson, A.W., 1985. On the use and significance of  
7 918 isentropic potential vorticity maps. *Q. J. R. Meteorol. Soc.* 111, 877–946.  
8 919 <https://doi.org/10.1002/qj.49711147002>  
9  
10 920 Hoskins, B.J., Valdes, P.J., 1990. On the Existence of Storm-Tracks. *J. Atmospheric Sci.*  
11 921 47, 1854–1864.  
12 922 [https://doi.org/10.1175/1520-0469\(1990\)047<1854:OTEOST>2.0.CO;2](https://doi.org/10.1175/1520-0469(1990)047<1854:OTEOST>2.0.CO;2)  
13  
14 923 James, I. N., 1987. Suppression of Baroclinic Instability in Horizontally Sheared Flows.  
15 924 *J. Atmospheric Sci.*, 44, 3710–3720,  
16 925 [doi:10.1175/1520-0469\(1987\)044<3710:SOBIH>2.0.CO;2](https://doi.org/10.1175/1520-0469(1987)044<3710:SOBIH>2.0.CO;2).  
17  
18 926 Kidston, J., Frierson, D.M.W., Renwick, J.A., Vallis, G.K., 2010. Observations,  
19 927 Simulations, and Dynamics of Jet Stream Variability and Annular Modes. *J. Clim.*  
20 928 23, 6186–6199. <https://doi.org/10.1175/2010JCLI3235.1>  
21  
22 929 Kidston, J., Vallis, G.K., 2012. The Relationship between the Speed and the Latitude of  
23 930 an Eddy-Driven Jet in a Stirred Barotropic Model. *J. Atmospheric Sci.* 69, 3251–  
24 931 3263. <https://doi.org/10.1175/JAS-D-11-0300.1>  
25  
26 932 Lau, N.-C., 1979. The Structure and Energetics of Transient Disturbances in the Northern  
27 933 Hemisphere Wintertime Circulation. *J. Atmospheric Sci.* 36, 982–995.  
28 934 [https://doi.org/10.1175/1520-0469\(1979\)036<0982:TSAEOT>2.0.CO;2](https://doi.org/10.1175/1520-0469(1979)036<0982:TSAEOT>2.0.CO;2)  
29  
30 935 Lee, S., Kim, H., 2003. The Dynamical Relationship between Subtropical and  
31 936 Eddy-Driven Jets. *J. Atmospheric Sci.* 60, 1490–1503.  
32 937 [https://doi.org/10.1175/1520-0469\(2003\)060<1490:TDRBSA>2.0.CO;2](https://doi.org/10.1175/1520-0469(2003)060<1490:TDRBSA>2.0.CO;2)  
33  
34 938 Li, C., Wettstein, J.J., 2011. Thermally Driven and Eddy-Driven Jet Variability in  
35 939 Reanalysis. *J. Clim.* 25, 1587–1596. <https://doi.org/10.1175/JCLI-D-11-00145.1>  
36  
37 940 Liang, X.S., 2016. Canonical Transfer and Multiscale Energetics for Primitive and  
38 941 Quasigeostrophic Atmospheres. *J. Atmospheric Sci.* 73, 4439–4468.  
39 942 <https://doi.org/10.1175/JAS-D-16-0131.1>  
40  
41 943 Liang, X.S., Anderson, D.G.M., 2007. Multiscale Window Transform. *Multiscale Model.*  
42 944 *Simul.* 6, 437–467. <https://doi.org/10.1137/06066895X>  
43  
44 945 Liang, X.S., Robinson, A.R., 2007. Localized multi-scale energy and vorticity analysis.  
45 946 *Dyn. Atmospheres Oceans* 44, 51–76.  
46 947 <https://doi.org/10.1016/j.dynatmoce.2007.04.001>  
47  
48 948 Liang, X.S., Robinson, A.R., 2005. Localized multiscale energy and vorticity analysis.  
49 949 *Dyn. Atmospheres Oceans* 38, 195–230.  
50 950 <https://doi.org/10.1016/j.dynatmoce.2004.12.004>  
51  
52 951 Lim, G.H., Wallace, J.M., 1991. Structure and Evolution of Baroclinic Waves as Inferred  
53 952 from Regression Analysis. *J. Atmospheric Sci.* 48, 1718–1732.  
54 953 [https://doi.org/10.1175/1520-0469\(1991\)048<1718:SAEOBW>2.0.CO;2](https://doi.org/10.1175/1520-0469(1991)048<1718:SAEOBW>2.0.CO;2)  
55  
56 954 Lindzen, R.S., Farrell, B., 1980. A Simple Approximate Result for the Maximum Growth  
57 955 Rate of Baroclinic Instabilities. *J. Atmospheric Sci.* 37, 1648–1654.

- 1  
2  
3  
4 956 [https://doi.org/10.1175/1520-0469\(1980\)037<1648:ASARFT>2.0.CO;2](https://doi.org/10.1175/1520-0469(1980)037<1648:ASARFT>2.0.CO;2)  
5 957 Lindzen, R.S., Holton, J.R., 1968. A Theory of the Quasi-Biennial Oscillation. *J.*  
6 958 *Atmospheric Sci.* 25, 1095–1107.  
7 959 [https://doi.org/10.1175/1520-0469\(1968\)025<1095:ATOTQB>2.0.CO;2](https://doi.org/10.1175/1520-0469(1968)025<1095:ATOTQB>2.0.CO;2)  
8 960 Lorenz, D.J., 2014. Understanding Midlatitude Jet Variability and Change Using Rossby  
9 961 Wave Chromatography: Wave–Mean Flow Interaction. *J. Atmospheric Sci.* 71,  
10 962 3684–3705. <https://doi.org/10.1175/JAS-D-13-0201.1>  
11 963 Lorenz, D.J., Hartmann, D.L., 2001. Eddy–Zonal Flow Feedback in the Southern  
12 964 Hemisphere. *J. Atmospheric Sci.* 58, 3312–3327.  
13 965 [https://doi.org/10.1175/1520-0469\(2001\)058<3312:EZFFIT>2.0.CO;2](https://doi.org/10.1175/1520-0469(2001)058<3312:EZFFIT>2.0.CO;2)  
14 966 Lorenz, E.N., 1955. Available Potential Energy and the Maintenance of the General  
15 967 Circulation. *Tellus* 7, 157–167.  
16 968 <https://doi.org/10.1111/j.2153-3490.1955.tb01148.x>  
17  
18 969 [Ma, J., X.S. Liang, 2017. Multiscale dynamical processes underlying the wintertime](#)  
19 970 [Atlantic blockings. \*J. Atmos. Sci.\*, 74, 3815-3831.](#)  
20  
21 971 Mak, M., M. Cai, 1989. Local Barotropic Instability. *J. Atmospheric Sci.*, 46, 3289–3311,  
22 972 doi:10.1175/1520-0469(1989)046<3289:LBI>2.0.CO;2.  
23  
24 973 Nakamura, H., 1992. Midwinter Suppression of Baroclinic Wave Activity in the Pacific.  
25 974 *J. Atmospheric Sci.* 49, 1629–1642.  
26 975 [https://doi.org/10.1175/1520-0469\(1992\)049<1629:MSOBWA>2.0.CO;2](https://doi.org/10.1175/1520-0469(1992)049<1629:MSOBWA>2.0.CO;2)  
27  
28 976 Novak, L., Ambaum, M.H.P., Tailleux, R., 2015. The Life Cycle of the North Atlantic  
29 977 Storm Track. *J. Atmospheric Sci.* 72, 821–833.  
30 978 <https://doi.org/10.1175/JAS-D-14-0082.1>  
31  
32 979 Orlandi, I., Chang, E.K.M., 1993. Ageostrophic Geopotential Fluxes in Downstream and  
33 980 Upstream Development of Baroclinic Waves. *J. Atmospheric Sci.* 50, 212–225.  
34 981 [https://doi.org/10.1175/1520-0469\(1993\)050<0212:AGFIDA>2.0.CO;2](https://doi.org/10.1175/1520-0469(1993)050<0212:AGFIDA>2.0.CO;2)  
35  
36 982 Orlandi, I., Katzfey, J., 1991. The Life Cycle of a Cyclone Wave in the Southern  
37 983 Hemisphere. Part I: Eddy Energy Budget. *J. Atmospheric Sci.* 48, 1972–1998.  
38 984 [https://doi.org/10.1175/1520-0469\(1991\)048<1972:TLCOAC>2.0.CO;2](https://doi.org/10.1175/1520-0469(1991)048<1972:TLCOAC>2.0.CO;2)  
39  
40 985 Papritz, L., S. Schemm, 2013. Development of an idealised downstream cyclone:  
41 986 Eulerian and Lagrangian perspective on the kinetic energy. *Tellus Dyn. Meteorol.*  
42 987 *Oceanogr.*, 65, 19539, doi:10.3402/tellusa.v65i0.19539.  
43  
44 988 Penny, S.M., Battisti, D.S., Roe, G.H., 2013. Examining Mechanisms of Variability  
45 989 within the Pacific Storm Track: Upstream Seeding and Jet-Core Strength. *J. Clim.*  
46 990 26, 5242–5259. <https://doi.org/10.1175/JCLI-D-12-00017.1>  
47  
48 991 Pierrehumbert, R.T., Swanson, K.L., 1995. Baroclinic Instability. *Annu. Rev. Fluid*  
49 992 *Mech.* 27, 419–467. <https://doi.org/10.1146/annurev.fl.27.010195.002223>  
50  
51 993 Plumb, R. A., 1983. A New Look at the Energy Cycle. *J. Atmospheric Sci.*, 40, 1669–  
52 994 1688, doi:10.1175/1520-0469(1983)040<1669:ANLATE>2.0.CO;2.  
53  
54 995 Plumb, R.A., 1985. An Alternative Form of Andrews’ Conservation Law for  
55 996 Quasi-geostrophic Waves on a Steady, Nonuniform Flow. *J. Atmospheric Sci.* 42,

1  
2  
3  
4  
5  
6  
7  
8  
9  
10  
11  
12  
13  
14  
15  
16  
17  
18  
19  
20  
21  
22  
23  
24  
25  
26  
27  
28  
29  
30  
31  
32  
33  
34  
35  
36  
37  
38  
39  
40  
41  
42  
43  
44  
45  
46  
47  
48  
49  
50  
51  
52  
53  
54  
55  
56  
57  
58  
59  
60

- 997 298–300.  
998 [https://doi.org/10.1175/1520-0469\(1985\)042<0298:AAFOAC>2.0.CO;2](https://doi.org/10.1175/1520-0469(1985)042<0298:AAFOAC>2.0.CO;2)
- 999 Rivière, G., B. L. Hua, P. Klein, 2003. Perturbation growth in terms of barotropic  
1000 alignment properties. *Q. J. R. Meteorol. Soc.*, 129, 2613–2635,  
1001 doi:10.1256/qj.02.106.
- 1002 ———, ———, and ———, 2004: Perturbation growth in terms of baroclinic alignment  
1003 properties. *Q. J. R. Meteorol. Soc.*, 130, 1655–1673, doi:10.1256/qj.02.223.
- 1004 Rivière, G., P. Arbogast, A. Joly, 2015. Eddy kinetic energy redistribution within  
1005 idealized extratropical cyclones using a two-layer quasi-geostrophic model: Eddy  
1006 kinetic energy redistribution within idealized extratropical cyclones using a  
1007 two-layer quasi-geostrophic model. *Q. J. R. Meteorol. Soc.*, 141, 207–223,  
1008 doi:10.1002/qj.2350.
- 1009 Robinson, W.A., 2000. A Baroclinic Mechanism for the Eddy Feedback on the Zonal  
1010 Index. *J. Atmospheric Sci.* 57, 415–422.  
1011 [https://doi.org/10.1175/1520-0469\(2000\)057<0415:ABMFTE>2.0.CO;2](https://doi.org/10.1175/1520-0469(2000)057<0415:ABMFTE>2.0.CO;2)
- 1012 Simmons, A.J., Hoskins, B.J., 1980. Barotropic Influences on the Growth and Decay of  
1013 Nonlinear Baroclinic Waves. *J. Atmospheric Sci.* 37, 1679–1684.  
1014 [https://doi.org/10.1175/1520-0469\(1980\)037<1679:BIOTGA>2.0.CO;2](https://doi.org/10.1175/1520-0469(1980)037<1679:BIOTGA>2.0.CO;2)
- 1015 Simmons, A.J., Hoskins, B.J., 1978. The Life Cycles of Some Nonlinear Baroclinic  
1016 Waves. *J. Atmospheric Sci.* 35, 414–432.  
1017 [https://doi.org/10.1175/1520-0469\(1978\)035<0414:TLCOSN>2.0.CO;2](https://doi.org/10.1175/1520-0469(1978)035<0414:TLCOSN>2.0.CO;2)
- 1018 Sinclair, M.R., Revell, M.J., 2000. Classification and Composite Diagnosis of  
1019 Extratropical Cyclogenesis Events in the Southwest Pacific. *Mon. Weather Rev.*  
1020 128, 1089–1105.  
1021 [https://doi.org/10.1175/1520-0493\(2000\)128<1089:CACDOE>2.0.CO;2](https://doi.org/10.1175/1520-0493(2000)128<1089:CACDOE>2.0.CO;2)
- 1022 Uppala, S.M., KÅllberg, P.W., Simmons, A.J., Andrae, U., Bechtold, V.D.C., Fiorino,  
1023 M., Gibson, J.K., Haseler, J., Hernandez, A., Kelly, G.A., Li, X., Onogi, K.,  
1024 Saarinen, S., Sokka, N., Allan, R.P., Andersson, E., Arpe, K., Balmaseda, M.A.,  
1025 Beljaars, A.C.M., Berg, L.V.D., Bidlot, J., Bormann, N., Caires, S., Chevallier, F.,  
1026 Dethof, A., Dragosavac, M., Fisher, M., Fuentes, M., Hagemann, S., Hólm, E.,  
1027 Hoskins, B.J., Isaksen, I., Janssen, P. a. E.M., Jenne, R., McNally, A.P., Mahfouf,  
1028 J.-F., Morcrette, J.-J., Rayner, N.A., Saunders, R.W., Simon, P., Sterl, A.,  
1029 Trenberth, K.E., Untch, A., Vasiljevic, D., Viterbo, P., Woollen, J., 2005. The  
1030 ERA-40 re-analysis. *Q. J. R. Meteorol. Soc.* 131, 2961–3012.  
1031 <https://doi.org/10.1256/qj.04.176>
- 1032 Vallis, G.K., Gerber, E.P., 2008. Local and hemispheric dynamics of the North Atlantic  
1033 Oscillation, annular patterns and the zonal index. *Dyn. Atmospheres Oceans,*  
1034 *Current Contributions to Understanding the General Circulation of the*  
1035 *Atmosphere Part 2* 44, 184–212. <https://doi.org/10.1016/j.dynatmoce.2007.04.003>
- 1036 Woollings, T., Hannachi, A., Hoskins, B., 2010. Variability of the North Atlantic  
1037 eddy-driven jet stream. *Q. J. R. Meteorol. Soc.* 136, 856–868.

- 1  
2  
3  
4 1038 <https://doi.org/10.1002/qj.625>  
5 1039 Xu, F., Liang, X.S., 2017. On the generation and maintenance of the 2012/13 sudden  
6 1040 stratospheric warming. *J. Atmos. Sci.*, 74, 3209-3228.  
7 1041 Zhang, Y., Yang, X.-Q., Nie, Y., Chen, G., 2012. Annular Mode–Like Variation in a  
8 1042 Multilayer Quasigeostrophic Model. *J. Atmospheric Sci.* 69, 2940–2958.  
9 1043 <https://doi.org/10.1175/JAS-D-11-0214.1>  
10 1044 Zhao, Y.-B., Liang X.S., 2018. On the inverse relationship between the boreal wintertime  
11 1045 Pacific jet strength and storm-track intensity. *J. Climate*,  
12 1046 <https://doi.org/10.1175/JCLI-D-18-0043.1>, in press.  
13  
14  
15 1047  
16  
17  
18  
19  
20  
21  
22  
23  
24  
25  
26  
27  
28  
29  
30  
31  
32  
33  
34  
35  
36  
37  
38  
39  
40  
41  
42  
43  
44  
45  
46  
47  
48  
49  
50  
51  
52  
53  
54  
55  
56  
57  
58  
59  
60